EFFECT OF CHANGING THE DIMENSION OF INITIAL DEBRIS MASS IN THE DYNAMICS OF LANDSLIDE GENERATED TSUNAMI

THESIS SUBMITTED TO
THE CENTRAL DEPARTMENT OF MATHEMATICS
INSTITUTE OF SCIENCE AND TECHNOLOGY
TRIBHUVAN UNIVERSITY
KATHMANDU, NEPAL

BY

GRISHMA ACHARYA

SUBMITTED FOR THE
PARTIAL FULFILLMENT OF THE REQUIREMENT FOR
THE MASTER IN SCIENCE (M.SC.) DEGREE
IN MATHEMATICS

JUNE, 2021

Thesis Grant
supported by
Nepal Academy of Science and Technology (NAST)

DEDICATION

To

My Father
Dev Kumar Acharya

With

My Mother
Dharma Sila Acharya

STUDENT'S DECLARATION

This thesis entitled "**Effect of Changing the Dimensions of Initial Debris Mass in the Dynamics of Landslide Generated Tsunami**", which has been submitted to the Central Department of Mathematics, Institute of Science and Technology (IOST), Tribhuvan University, Nepal for the partial fulfillment of the Master in Science (M.Sc.) Degree in Mathematics, is a genuine work that I carried out under my supervisor **Dr. Jeevan Kafle** and that no sources other than those listed in the Bibliography have been used in this work. Moreover, this work has not been published or submitted elsewhere for the requirement of any degree programme.

Grishma Acharya
Batch: 2074
TU Registration Number: 5-2-0002-0067-2013
Date: June 25, 2021

RECOMMENDATION

This is to recommend that Mr. **Grishma Acharya** has prepared this thesis entitled "**Effect of Changing the Dimensions of Initial Debris Mass in the Dynamics of Landslide Generated Tsunami**" for the partial fulfillment of the Master in Science (M.Sc.) in Mathematics under my supervision. To my knowledge, this work has not been submitted for any other degree. He has fulfilled all the requirements laid down by the Central Department of Mathematics, Institute of Science and Technology (IOST), Tribhuvan University (TU), Kirtipur for the submission of the thesis for the partial fulfillment of M.Sc. Degree in Mathematics.

.....

(Dr. Jeevan Kafle)

Supervisor

Assistant Professor

Central Department of Mathematics

Tribhuvan University,

Kirtipur, Kathmandu, Nepal

Date: June 25, 2021

LETTER OF APPROVAL

We certify that the Research Evaluation Committee of the Central Department of Mathematics, Tribhuvan University, Kirtipur approved this research work entitled "**Effect of Changing the Dimensions of Initial Debris Mass in the Dynamics of Landslide Generated Tsunami**" carried out by Mr. **Grishma Acharya** in the scope and generality as a thesis in the partial fulfillment for the requirement of the M.Sc. degree in Mathematics.

.....

(Dr. Ganga Ram Phaijoo)
External Examiner
Assistant Professor
Department of Mathematics
School of Science, Kathmandu University
Dhulikhel, Kavre, Nepal.
Date: June 25, 2021

.....

(Dr. Jeevan Kafle)
Supervisor
Assistant Professor
Central Department of Mathemarics
Tribhuvan University, Kirtipur, Nepal
Date: June 25, 2021

.....

Prof. Dr. Tanka Nath Dhamala
(Head of Department)
Central Department of Mathematics
Institute of Science & Technology
Tribhuvan University Kirtipur, Kathmandu, Nepal.
Date: June 25, 2021

ACKNOWLEDGMENTS

First and foremost, I would like to express the deepest appreciation, gratitude and indebtedness to my supervisor Dr. Jeevan Kafle for his inspiration, motivation, supervision and full support. I am very Thankful for his time and unbelievable amount of scientific support for this research work, research opportunities. Moreover, his continuous guidance, effort and suggestions which have been very helpful for me to complete this work successfully. I would also like to express my gratitude and indebtedness towards my respected teachers Dr. Parameshwari Kattel, Dr. Puskar Raj Pokhrel. and Mr. Bekha Ratna Dangol for their valueable time and endless support.

I have also been benefited from comments and discussions at various stages of this thesis from my colleagues Mr. Bhogendra Kumar Thakur and Mr. Hari Prasad Gaire. I am especially thankful to them, not only for the enriching conversations, but because they have been a wonderful company during this work. I am also thankful to my sister Miss Jeebita Acharya for her kind support for this work. I gratefully acknowledge the financial support provided by the Nepal Academy of science and technology (NAST).

It is my pleasure to thank the Central Department of Mathematics, Tribhuvan University for the support provided to me so far. I also express my sincere gratitude to Nepal Academy of science and technology (NAST), Nepal. Finally, I would like to thank my family for their continuous love, care and support during this research period.

Grishma Acharya

Date: June, 2021

ABSTRACT

Debris flow is a traveling mass of loose mud, soil, air, water and sand that moves down a slope caused due to gravity. When debris flows, landslides, or any gravitational mass flows hit closed or partially open water sources such as seas, oceans, fjords, hydraulic reservoirs, mountain lakes, bays and landslide dams, it results in tsunami (impulse water waves) by transforming their impact energy to water body, potentially causing damages of infrastructures and human casualties both near field and the distant coastlines. The degree of hazard depends on the scale, types, location and process of the landslide. Volume or size of the initial debris mass that fails in the slope, is one of the dominant factors in accelerating the splash strength or intensity, the propagation and amplitudes of the subsequent water waves and potential dam breach or water spill over. Here, we numerically integrate the two-phase mass flow model [61] for quasi three dimensional, high-resolution simulation results with variation of size of the two-phase initial landslide or debris both longitudinally and laterally. In our numerical experimental results, we observe fundamentally different solid and fluid wave structures in the reservoir, and the dynamics of submarine mass flow for different volumes of the release mass by extending or contracting the base area along down-slope and/or cross-slope directions. The simulation results show that tsunami amplitudes and run out extents are rapidly increased when the volume of initial release mass in the form of a triangular wedge is enlarged by increasing the base area through the increment of the length and breadth of the release base. This study can be an instructive tool to develop and implement tsunami hazard mitigation measures to enhance public safety and reduce potential loss.

LIST OF ACRONYMS AND ABBREVIATIONS

TVD: Total Variation Diminishing

NOC: Non Oscillatory Central

LIST OF SYMBOLS

$\mathcal{A}$	mobility number.
b	basal surface of flow.
C_{DG}	generalized drag coefficient.
$\mathcal{C}$	virtual mass coeffi cient.
f	stands for fluid phase.
s	stands for solid phase.
$\mathcal{F}$	fluid-like contribution in generalized drag:C_{DG}.
$\mathcal{G}$	solid-like contribution in generalized drag:C_{DG}.
g	gravity constant.
$\mathbf{g}$	accelation due to gravity.
g^x, g^y, g^y	components of gravitational acceleration.
h	debris flow height, $h = h_s + h_f$.
h_f	fluid contribution to flow height, $h_f = \alpha_f h$.
h_s	solid contribution to flow height, $h_s = \alpha_s h$.
$\mathbf{I}$	identity matrix.
m_f	fuid momentum flux, $m_f = \alpha_f h u_f$.
m_s	solid momentum flux, $m_s = \alpha_s h u_s$.
M	a parameter depending on Reynolds number.
N_R	reynolds number; $N_R = \sqrt{gL}\rho f H/\alpha_f \eta_f$.
$N_{R_\mathcal{A}}$	quasi-Reynolds number/mobility number.
p	fluid presure.
$\mathcal{P}$	parameter combining solid-like and fluid-like drag contributions.
p_{b_f}	effective fluid pressure at base.
p_{b_s}	effective solid pressure at base.
Re_p	particle Reynolds number, $Re_p = \rho_f d\mathcal{U}_T/\eta_f u$.
$\mathbf{S}$	shear stress.
S	source terms.
s	solid-phase.
t	time.
$\mathbf{T}$	total stress.
$\mathbf{u}_f$	velocity for fluid, $\mathbf{u}_f = (u_f, v_f, w_f)$.
$\mathbf{u}_s$	velocity for solid, $\mathbf{u}_s = (u_s, v_s, w_s)$.

$\mathcal{U}_s$	particle sedimentation velocity.
$\mathcal{U}_T$	terminal velocity of a particle.
x, y, z	spatial coordinates.
α_f	volume fraction for fluid.
α_s	volume fraction for solid.
α	submerge factor.
β_{x_s}, β_{y_s}	lateral hydraulic pressure parameters for solid.
β_{x_f}, β_{y_f}	lateral hydraulic pressure parameters for solid.
γ	density ratio, $\gamma = \rho_f/\rho_s$h.
δ	basal friction angle.
ε	aspect ratio, $\varepsilon = H/L$.
ζ	channel slope angle.
η_f	fluid viscosity.
μ	basal friction coefficient, $\mu = \tan\delta$.
ξ	vertical distribution of α_s.
ρ	debris bulk density.
ρ_s	solid-phase density.
ρ_f	fluid-phase density.
ϕ	internal friction angle.

List of Figures

1.1 A schematic diagram of different stages involved in a Subaerial-landslide (SAL) generated tsunami event 2
1.2 Sun Koshi River **left:** before landslide on June 2013 and **right:** after the landslide on August 2, 2014. 4
1.3 Vajont dam and reservoir **A**: before the landslide, **B**: after the landslide. . 5

3.1 A sketch showing the initial set up with the initial release and the fluid reservoir. 13
3.2 **Reference Simulation** (Base of the initial debris mass at $75 \leq x \leq 125$ m, $-25 \leq y \leq 25$ m). **A:** Total height of the debris mass and tsunami waves. Tsunami is generated, amplified and propagates as time elapses. **B:** Evolution of the solid phase in the debris mixture in subaerial part as well as in the reservoir. The solid phase advects and disperses both in subaerial slope and the bathymetry, with the formation of special solid wave. **C:** Evolution of the fluid constituent in the debris mixture and the reservoir. Tsunami amplitude in each time slice is the excess fluid height over the initial fluid height (25 m) in the reservoir. 15
3.3 **Reduced volume of the initial debris mass** (Base of the initial debris mass at $85 \leq x \leq 115$ m, $-25 \leq y \leq 25$ m) **A:** Total height of the debris mass and tsunami waves. As time elapses, less intensified tsunami is produced that propagates less cross-slope and downslope than in Fig. 3.2. **B:** Evolution of the solid phase in the debris mixture in the subaerial as well as in the reservoir. The solid part of the debris body is less dispersed that also moves less downslope, but the solid maximum is wider than in Fig. 3.2. 18

3.4 **Increased volume of initial debris mass** (Base of the initial debris mass at $65 \leq x \leq 135$ m, $-25 \leq y \leq 25$ m) **A:** Total height of the debris mass and tsunami waves. As time elapses, more intensified tsunami is produced that propagates more cross-slope and downslope than in Fig. 3.2 **B:** Evolution of the solid phase. In this case, the submarine mass reaches the right coast faster (already at $t = 7$ s) than in Fig. 3.2. 20

3.5 **Reduced volume of initial debris mass along cross-slope direction** (Base of the initial debris mass at $75 \leq x \leq 125$ m, $-15 \leq y \leq 15$ m) **A:** Total height of the debris mass and tsunami waves. As time elapses, less intensified tsunami is produced that propagates less cross-slope and down slope than in Fig. 3.2. **B:** Evolution of the solid phase in the subaerial slope and in the reservoir. The flowing mass attains less velocity than in Fig. 3.2. 22

3.6 **Increased volume of initial debris mass along Cross-slope direction** (Sase of the initail debris mass at $75 \leq x \leq 125$ m, $-35 \leq y \leq 35$ m) **A:** Total height of the debris mass and tsunami waves. As time elapses, a bit more intensified tsunami wave is produced that propagates more cross-slope and downslope then in Fig. 3.2. **B:** Evolution of the solid phase in the debris mixture. In this case, the submarine mass just starts hitting the right coast of the reservoir at $t = 9$ s, whereas in Fig. 3.2 it was more upslope of right coast of the reservoir. 24

3.7 **Reduced volume of the initial debris mass** (Base of the initial debris mass at $85 \leq x \leq 115$ m, $-15 \leq y \leq 15$ m) **A:** Total height of the debris mass and tsunami waves. As time elapses, less intensified tsunami is produced that propagates less cross-slope and downslope than in Fig. 3.2. **B:** Evolution of the solid phase. The solid part of the debris body is less dispersed that also moves less downslope. 26

3.8 **Increaded volume of the initial debris mass** (Base of the initial debris mass at $65 \leq x \leq 135$ m, $-35 \leq y \leq 35$ m) **A:** Total height of the debris mass and tsunami waves. As time elapses, more intensified tsunami is produced that propagates more cross-slope and downslope than in Fig. 3.2. **B:** Evolution of the solid phase in the debris mixture. In this case, the submarine mass reaches the right coast faster than in Fig. 3.2 (already at t = 7 s). 28

3.9 **Comparison of tsunami amplitudes.** 31

3.10 **Comparison of solid maximum positions for different volumes at $t = 0$ s to $t = 9$ s.** 31
3.11 **Comparison of solid front positions for different volumes at $t = 0$ to $t = 9$ s.** 32

List of Tables

3.1 Comparison of tsunami amplitudes in case of different volume of initial release mass at time t = 7 s. 29
3.2 Comparison of maximum solid height in case of different volume of initial debris configurations at time t = 9 s 30

Contents

DEDICATION iv

STUDENT DECLARATION v

RECOMMENDATION vi

LETTER OF APPROVAL vii

ACKNOWLEDGMENTS viii

ABSTRACT ix

LIST OF ACRONYMS AND ABBREVIATIONS x

LIST OF SYMBOLS xi

LIST OF FIGURES xv

LIST OF TABLES xvi

1 INTRODUCTION 1

1.1 Background 1

1.1.1 Debris flow 1

1.1.2 Tsunami 2

1.1.3 Landslide-generated Tsunami 3

1.2 Motivation 4

1.3 Significance / Rationale of the study 5

1.4 Literature Review 6

1.5 Objectives 8

1.6 Thesis Structure 8

2 GOVERNING EQUATIONS AND NUMERICAL METHODS 9
2.1 Model Equations 9

3 RESULTS OF NUMERICAL EXPERIMENTS AND DISCUSSION 13
3.1 Reference Simulation 14
3.2 Variation of volume of initial debris mass by changing its extent along $\boldsymbol{x}$-direction 17
3.2.1 Reduction of volume of the initial mass 17
3.2.2 Increment of volume of the initial mass 19
3.3 Variation of volume of initial debris mass by changing its extent along $\boldsymbol{y}$-direction 21
3.3.1 Reduction of volume of the initial debris mass 21
3.3.2 Increment of volume of the initial debris mass 23
3.4 Variation of volume of initial release mass by reducing its extent along both $\boldsymbol{x}$- and $\boldsymbol{y}$- directions 25
3.5 Variation of volume of initial debris mass by increasing its extent along both $\boldsymbol{x}$- and $\boldsymbol{y}$-directions 27
3.6 Comparisons of tsunami amplitudes and run-out scenarios 29
3.7 Comparisons of Solid front position, Position of Maximum solid heights and Tsunami Amplitudes 31

4 SUMMARY 34

LIST OF SUBMITTED PAPER 35

LIST OF PRESENTATIONS 36

REFERENCES 43

Chapter 1

INTRODUCTION

1.1 Background

Geophysical mass flows in mountainous and coastal regions include subaerial or submarine landslides, debris flows, mud flows, avalanches, lahars, pyroclastic flows and tsunamis [15, 17, 45, 64]. These catastrophic events show variable flow behaviour, and are generally multiphase, and especially the interaction between the phases during the flow makes the flow rheologically complicated adding high complexity to scientific studies [32, 56, 61, 62, 78]. Water-saturated landslides or debris flows generally occur in steep mountain slopes and channels due to heavy rain and snow-melts. The mechanically weaker viscous fluid and stronger solid particles possess different physics of flow during the flow [22, 25, 26, 29, 34, 35, 56, 57, 72]. Water waves or tsunami generated by the plunging of landslides into natural lakes and reservoirs might cause serious damages during run up shores or against dams [6, 42, 76]. It is very important to have advanced knowledge of evolution of the solid and fluid-phases along with the huge landslides in the coastal areas and particle transport in hydraulic plants from the environmental and industrial point of view also [62]. Many researchers have been challenged to figure out the physics of such complex events, which is still poorly understood due to its multiple complexities including their dimensions, phases and mechanics [62]. The high Himalayan regions are increasingly prone to devastating snow avalanches, landslides, debris flows and rockfalls [25].

1.1.1 Debris flow

Debris flows are rapidly moving landslides that are unusually dangerous to life and property. It moves with tremendous speed, demolishing the objects in their paths, and often bang without warning. The speed and volume of debris flows make them very dangerous.

Every year, worldwide, many people are killed by debris flows. They occur in a wide variety of environments throughout the world. Debris flows generally occur during periods of intense rainfall or rapid snow melt and usually start on hillsides or mountains. When debris flows enters a steep stream channel, it travel for several miles, impacting areas unaware of the hazard. Debris flows is a type of landslide that is sometimes referred to as mudslides, mudflows, lahars, or debris avalanche. This hazard can be reduced by identifying areas that can potentially produce debris flows, educating people who live in those areas and govern them, limiting development in debris flow hazard areas, and developing a debris flow mitigation plan [19, 24, 43].

1.1.2 Tsunami

The word 'tsunami' derive from the Japanese word with the sense 'harbor wave'. Tsunamis are long water waves which is caused by a sudden disturbance of the floor or surface of ocean, bays, sea or lakes, fjords, hydraulic reservoirs or mountain lakes and landslide dams which is generally caused by sea floor deformation, landslides, earthquakes, volcanic eruptions, slumps, shore instabilities, subsidence, meteorite impacts and underwater explosions asteroid impacts, or landslides [5, 47, 52, 77]. Depending on the initial position of the triggered landslide relative to the water surface, the landslide-water interaction can be categorized as subaerial, partially submerged and submarine landslides [9, 31, 33, 52]. Subaerial and submarine landslides are also a cause of tsunamis as they transfer their impact energy to water body (e.g., ocean, sea, bays, fjords, hydraulic reservoirs or mountain lakes and landslide dams) [42, 47, 49, 50, 77]. This transfer of energy results in

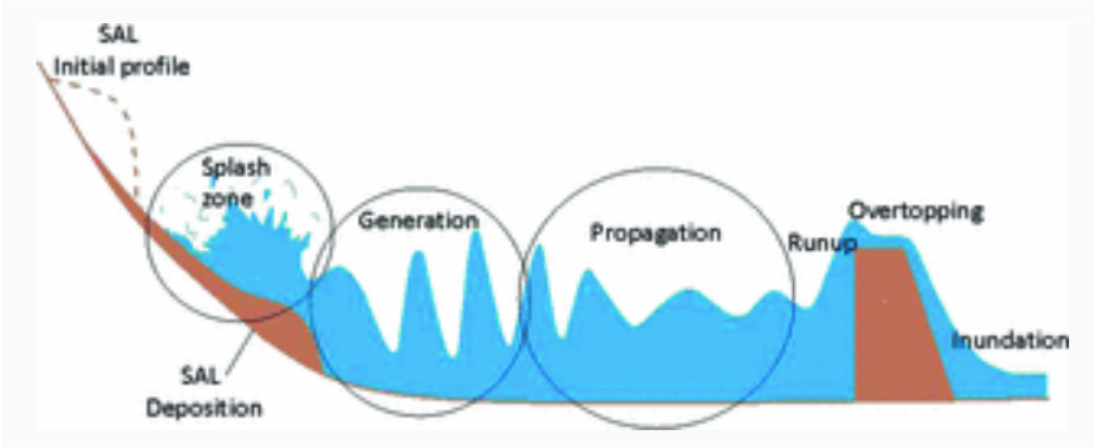

Figure 1.1: A schematic diagram of different stages involved in a Subaerial-landslide (SAL) generated tsunami event [1].

impulsive water waves that cause devastation on the costal region mainly due to run-up along the shoreline, overtopping of dams, subsequent dam breaking [50] and subsequent flooding [77]. The significant energy carried by tsunami propagation can cause damages and casualties both near field as well as distant coastlines such as breakwaters, seawalls, piers, submarine cables, bridges/pillars, artificial floating island/airport, and fish and wind farms [42]. Tsunami wave shoaling, diffraction, refraction and wave breaking depend upon the initial volume of the landslide mass, bathymetry and the topography as well as vulnerability of the coastal region [51].

Tsunamis can be classified as local, regional and distant depending on the distance of the tsunami from its source [2].

- A tsunami that originates from within about 100 km or less than 1 hour tsunami travel time from the impacted coastline is known as a *local tsunami*. Local tsunamis can result in a significant number of casualties since authorities have little time to warn the vulnerable population.

- A *regional tsunami* is the one that is capable of destructing in a particular geographical region, generally within 1,000 km from its source.

- A tsunami originating from a source, generally more than 1,000 km or more than 3 hours of travel time from the impacted coastline is called a *distant tsunami*. These tsunamis have the ability to cause widespread destruction, not only in the immediate regions but across an entire ocean .

1.1.3 Landslide-generated Tsunami

Landslides and volcanoes are the most common sources of tsunamis after earthquakes. Among the tsunamis caused by different geophysical events, landslide generated tsunamis are much more localized and may cause more local threats than earthquake-generated tsunamis although they are less frequent [14, 47, 67, 73]. The induced water wave characteristics like amplitudes, velocity, wavelength and period, are governed by the water body geometry, depth, volume, and dimensions, as well as the slide characteristics, underwater travel time, and the slope angle [77]. The landslide tsunami generation and propagation process may involve various phenomena in chain: landslide triggering, landslide dynamics, energy transfer from landslide to water body, tsunami wave generation, submarine landslide run out, potential obstacle interactions, tsunami propagation in water body and wave run up along the shores [49, 50, 77].

The hazard posed by submarine landslides varies according to the landslide scale, location, type and process. Even small submarine landslides can become dangerous if they occur in coastal areas. The tsunami prevention system consists of forecasting, warning, evacuation, public education, drills, inheritance of disaster culture, and the relief operation after disaster [70]. Although there were substantial attempts made in the past, all these events and their associated dynamics, and impacts are yet to be satisfactorily investigated further. The development and applications of the mitigation measures need further improvements.

1.2 Motivation

A huge landslide in Sun Koshi River in Nepal about 80 km east of Kathmandu on August 2, 2014 claimed over 300 people missing or dead, and blocked the river to submerge many houses and devastate a small hydropower station 3 km upstream [1]. A seismic magnitude of 7.9 Richter scale earthquake on the Fairweather Fault triggered a rock avalanche at the head of Lituya Bay, Alaska on July 9, 1958. The landslide produced a wave that ran up 524 meters (1,719 feet) on the opposite shore and produced a 30-meter-high wave through Lituya Bay, sinking two fishing boats and killed two people. It is considered as the greatest tsunami ever recorded [10].

For an instance, approximately 2.6×10^8 m^3 of rock broke off from the slope of Monte Toc,

Figure 1.2: Sun Koshi River **left:** before landslide on June 2013 and **right:** after the landslide on August 2, 2014 [1].

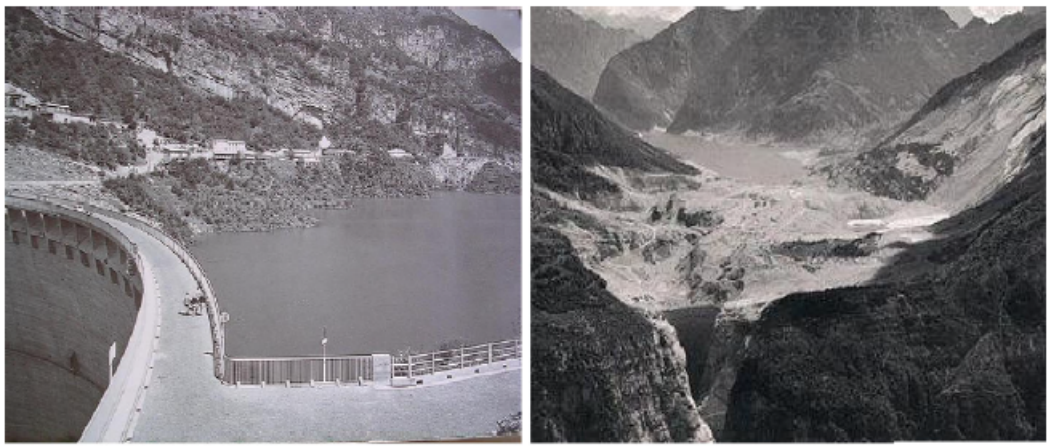

Figure 1.3: Vajont dam and reservoir **A**: before the landslide, **B**: after the landslide [16].

and plunged into the reservoir of Vajont Dam (Italy) on October 9, 1963 (figure 1.3A). The landslide impact induced in a massive wave of at least 5×10^9 m^3 of water (Fig. 1.3B). The subsequent flood completely devastated the village of Longarone in the Piave Valley and claimed approx. 2000 human lives. Since then such displacement waves have been acknowledged as a serious geohazard for dams [16, 18].

1.3 Significance / Rationale of the study

The observation and understanding of tsunami intensity, propagation and the submarine mass movement is useful for hazard mitigation in the tsunami-prone zones [33]. The initial debris play important roles in the degree or intensity of splash on impact amplitudes and propagation speeds of the resulting water waves and possible dam breaching or over spilling of water. This study helps us to know how the positions of initial debris mass on the inclined slope influence the splash, tsunami generation and submarine debris mass movements. This includes mass spreading and acceleration in both the subaerial and submarine environment impact and submergence times and scaling. The impact and submarine stoppage times and describing the splash zone and far field dynamics will be determined [31]. The results is applicable for studying the stability of reservoir dams, embankments and slopes caused by fluctuating water levels during landslides impact [39]. The study of the effects of variation of the size of initial debris mass can be useful for the mitigation of the hazard posed by tsunami and submarine mass movements for the coastal and mountain population and infrastructures.

1.4 Literature Review

In the past, various significant fundamental research activities were done on single-phase debris flows [3, 54], single-phase dry granular avalanches [12, 20, 21, 63, 68], mixture flows [22, 23, 66], two-phase debris flows [56], and also with two-layered model [7]. Several analytical methods were also proposed to analyze the wave run-up [53], velocity of submerged solid [55, 75], and wave velocity along a plane beach [67]. Most of the numerical experiments for landslide and tsunami found in existing literature are based on effectively single-phase shallow water and/or granular flow models. Employing Mohr-Coulomb frictional rheology and continuum mechanics, Savage and Hutter [68] developed a depth-averaged model to describe quasi two-dimensional flow of granular material down a slope assuming basal friction angle less than internal frictional angle [13, 63, 64, 68, 69, 71]. Further extensions were made for two and three dimensions [11, 63]. Although Iverson [22] and Iverson and Denlinger [23] and their extensions by Pudasaini et al. [66] incorporated basal opening fluid pressure to include viscous effects, they are merely quasi two-phase, or effectively single-phase models as they fail to address the coupling and cross-coupling of solid and fluid phase velocities.

Pitman and Le [56] included drag force to describe flows in their two-fluid model, the viscous fluid effects were neglected, and the drag force was simple. Wave generation and propagation were studied by Ma et al. [48] through a shock-capturing three-dimensional non-hydrostatic dispersive surface wave model, whereas by Ma et al. [47] through a two-layer depth-averaged computational model. In the simulations of Grilli et al. [14], coastal tsunami hazards are assessed by employing Bossinesq long wave model. Walder et al. [74] correlated the amplitude and shape of the wave generated in near field with the reservoir depth, the volume of the release mass, and the time through which submerged landslide remain in motion. While most of the research in recent years are found to be based on single- and quasi two-phase landslides, debris avalanches and debris flows and induced tsunami, Pudasaini [61] made further progress by developing a two-phase mass flow model that accounts for strong interactions between the constituent phases along with the inclusion of buoyancy, and also other three dominant physical aspects of two-phase mass flow such as virtual mass force, generalized drag, and non-Newtonian viscous stress induced by the changing sediment concentration in the debris mixture during the flow.

Pudasaini [61, 62] simulated the two-phase debris flow to reveal the explicit evolutions of the constituent phases as well as the debris bulk mixture for both subaerial and submarine environments. In particular, Pudasaini [62] simulated two-phase and geometrically two-dimensional flows where the flows impacts the quiescent fluid reservoir to generate

waves and the flow of submarine debris mass slides further along the bathymetric surface. For idealized geometry, Kafle [25] and Kafle et al. [31] presented further simulation results for two-phase and geometrically three-dimensional subaerial flows impacting a fluid reservoir to reveal the splash, tsunami generation, and submarine debris mass movements. Moreover, they analyzed in detail to study the influence of the variation of the positions of release mass influences in the splash, tsunami generation, and submarine debris mass movements. Kafle et al. [31] additionally showed that submerge time scaling for a deformable two-phase debris deviates substantially from the those for a non-deformable solid. Kafle and Tuladhar [33] simulated the interaction of a partially submerged landslide with a reservoir to reveal different evolutions and dynamics of surface fluid waves, and solid waves at the bathymetry. Kafle et al. [28] simulated by mounting obstacles in the shape of spherical bumps of different sizes, and numbers at different positions of subaerial slopes as well as inside reservoir, and observed the effects of obstacles in the tsunami intensity and speeds. De Lange et al. [44] investigated the effects of volume and composition of debris flow, and subaerial outflow slope on wave celerity and amplitude in a small-scaled physical set up consisting of an inclined outflow channel that runs into a three-dimensional water reservoir.

Recently Kafle et al. [30] simulated the topographical effect of slope changes in the dynamics of landslide generated water waves and submarine mass flows. Liu et al. [46] derive a simple model to evaluate the performance of an intercept dam for debris flow mitigation. In this model a two-phase model is combined with the dam moment balance theory to describe the condition of debris flow and the dam. A two-layer non-hydrostatic landslide model for tsunami generation on irregular bathymetry numerical discretization and model validation is defined by Zhang et al. [79] in 2021. In this model the hyperbolicity of the governing equations is preserved. Franci et al. [8] performed 3D simulation of Vajont disaster part two of Multi-failure scenarios. Through several numerical experiments, Kafle et al. [30] analyzed the effects of slope changes in different parts of the upstream subaerial slopes in the dynamics of fluid and solid waves. Employing the general two-phase mass flow model of Pudasaini [61], there are significant studies related to two-phase debris flow dynamics, glacial lake outburst floods and process chains [27, 37, 49, 50]. The model has been successful to simulate the two-phase debris flow-structure-interactions and resulting flow redirection and phase separation [35, 36, 38]. The model has further been employed to construct quasi two-phase bulk mixture mass flow models along with the simulations and parameter analyses [40, 41, 58, 60, 59] .

1.5 Objectives

The following are the major objectives of this proposed research work:

Objective-I: To develop an understanding of the concept of the dynamics of landslide generated tsunami.

Objective-II: To perform a reference simulation/experiment of subaerial and submarine two-phase mass flows when initial debris mass is at position $(75 < x < 125, -25 < y < 25)$ m and study the dynamics and impact.

Objective-III: To perform experiments and analyze in detail, the effects of the variation of length of initial debris mass along downslope direction, e.g.,$(85 < x < 115, -25 < y < 25)$,$(65 < x < 135, -25 < y < 25)$, etc., and compare the results with the reference simulation/experiment.

Objective-IV: Similar experiments and studies are to be performed by varying the length of initial debris mass along crossslope direction, e.g., $(75 < x < 115, -15 < y < 15)$, $(75 < x < 125, -35 < y < 35)$, etc., and results are compared with the previous cases.

Objective-V: To perform the simulation of the variation of initial debris mass along both cross slope and down slope direction, e.g.,$(85 < x < 115, -15 < y < 15)$, $(65 < x < 135, -35 < y < 35)$, etc., and compare the results with the reference simulation.

Objective-VI: To compare Tsunami amplitude, solid front position and maximum solid height of all simulation with reference simulation.

1.6 Thesis Structure

Chapter 1 gives a background of the work along with general introduction of the work. In Chapter 2, governing equations for debris flow and landslide generated tsunami is presented. In Chapter 3. detailed discussions on advanced three dimension simulation of debris mass with variation in volume of initial debris mass and comparison between Tsunami intensity, maximum solid height and solid front position with reference simulation and Chapter 4 contains the summary of this work.

Chapter 2

Governing Equations and Numerical Methods

2.1 Model Equations

In this section, we mention the employed general two-phase mass flow model, developed by Pudasaini [61]. In a two-phase debris mixture, sediments constitute the solid phase (s) and the viscous water as the fluid phase (f), with different material properties. In fluid, the stresses are isotropic and the fluid density and viscosity are respectively represented by ρ_f and viscosity η_f, whereas the material density ρ_s, internal friction angle ϕ, the basal friction angle δ, and anistropic stress distribution through the lateral earth pressure coefficient K characterize the solid phase. In the following model equations (2.1)-(2.6), x, y and z are coordinates along the downslope, cross-slope and the surface normal directions, respectively; g^x, g^y and g^z are the respective components of gravitational acceleration. The depth-averaged velocities for solid $\mathbf{u}_f = (u_f, v_f)$ and for fluid $\mathbf{u}_s = (u_s, v_s)$ have the components in the downslope (x) and the cross-slope (y) directions, respectively. The debris flow depth is h; α_s and $\alpha_f = 1 - \alpha_s$ are the solid and fluid volume fractions in the mixture at any time t, so that the solid contribution to flow depth is $\alpha_s h$ and the fluid contribution is of $\alpha_f h$. The following two equations are mass balances for solid and fluid [61]:

$$\frac{\partial}{\partial t}(\alpha_s h) + \frac{\partial}{\partial x}(\alpha_s h u_s) + \frac{\partial}{\partial y}(\alpha_s h v_s) = 0, \tag{2.1}$$

$$\frac{\partial}{\partial t}(\alpha_f h) + \frac{\partial}{\partial x}(\alpha_f h u_f) + \frac{\partial}{\partial y}(\alpha_f h v_f) = 0. \tag{2.2}$$

The non-linear partial differential equations representing momentum balances for solid and fluid in the downslope and the cross-slope directions are given by [61]:

$$\frac{\partial}{\partial t}\left[\alpha_s h\big(u_s-\gamma\mathcal{C}\left(u_f-u_s\right)\big)\right]+\frac{\partial}{\partial x}\left[\alpha_s h\left(u_s^2-\gamma\mathcal{C}(u_f^2-u_s^2)+\frac{1}{2}\beta_{x_s}h\right)\right] \tag{2.3}$$
$$+\frac{\partial}{\partial y}\left[\alpha_s h\big(u_s v_s-\gamma\mathcal{C}(u_f v_f-u_s v_s)\big)\right]=hS_{x_s},$$

$$\frac{\partial}{\partial t}\left[\alpha_s\, h\left(v_s-\gamma\mathcal{C}\left(v_f-v_s\right)\right)\right]+\frac{\partial}{\partial x}\left[\alpha_s h\big(u_s\, v_s-\gamma\mathcal{C}(u_f v_f-u_s v_s)\big)\right] \tag{2.4}$$
$$+\frac{\partial}{\partial y}\left[\alpha_s h\left(v_s^2-\gamma\mathcal{C}(v_f^2-v_s^2)+\frac{1}{2}\beta_{y_s}h\right)\right]=hS_{y_s},$$

$$\frac{\partial}{\partial t}\left[\alpha_f h\left(u_f+\frac{\alpha_s}{\alpha_f}\mathcal{C}(u_f-u_s)\right)\right]+\frac{\partial}{\partial x}\left[\alpha_f h\left(u_f^2+\frac{\alpha_s}{\alpha_f}\mathcal{C}(u_f^2-u_s^2)+\frac{1}{2}\beta_{x_f}h\right)\right] \tag{2.5}$$
$$+\frac{\partial}{\partial y}\left[\alpha_f h\left(u_f v_f+\frac{\alpha_s}{\alpha_f}\mathcal{C}(u_f v_f-u_s v_s)\right)\right]=hS_{x_f},$$

$$\frac{\partial}{\partial t}\left[\alpha_f h\left(v_f+\frac{\alpha_s}{\alpha_f}\mathcal{C}(v_f-v_s)\right)\right]+\frac{\partial}{\partial x}\left[\alpha_f h\left(u_f v_f+\frac{\alpha_s}{\alpha_f}\mathcal{C}(u_f v_f-u_s v_s)\right)\right] \tag{2.6}$$
$$+\frac{\partial}{\partial y}\left[\alpha_f h\left(v_f^2+\frac{\alpha_s}{\alpha_f}\mathcal{C}(v_f^2-v_s^2)+\frac{1}{2}\beta_{y_f}h\right)\right]=hS_{y_f},$$

in which

$$\beta_{x_s}=\varepsilon K_x p_{b_s},\ \beta_{y_s}=\varepsilon K_y p_{b_s},\ \beta_{x_f}=\beta_{y_f}=\varepsilon p_{b_f},\ p_{b_f}=-g^z,\ p_{b_s}=(1-\gamma)p_{b_f}.$$

In the above equations, p_{b_f} and p_{b_s} denote the effective fluid and solid pressures at the base. In the right hand side of (2.3)-(2.6), the source terms are further described as [61]:

$$S_{x_s}=\alpha_s\left[g^x-p_{b_s}\left(\frac{u_s}{|\mathbf{u_s}|}\tan\delta+\varepsilon\frac{\partial b}{\partial x}\right)\right]-\varepsilon\alpha_s\gamma p_{b_f}\left[\frac{\partial h}{\partial x}+\frac{\partial b}{\partial x}\right]+C_{DG}(u_f-u_s)\big|\mathbf{u}_f-\mathbf{u}_s\big|^{J-1}, \tag{2.7}$$

$$S_{y_s}=\alpha_s\left[g^y-p_{b_s}\left(\frac{v_s}{|\mathbf{u_s}|}\tan\delta+\varepsilon\frac{\partial b}{\partial y}\right)\right]-\varepsilon\alpha_s\gamma p_{b_f}\left[\frac{\partial h}{\partial y}+\frac{\partial b}{\partial y}\right]+C_{DG}(v_f-v_s)\big|\mathbf{u}_f-\mathbf{u}_s\big|^{J-1}, \tag{2.8}$$

$$S_{x_f} = \alpha_f \Bigg[g^x - \varepsilon \Bigg[\frac{1}{2} p_{b_f} \frac{h}{\alpha_f} \frac{\partial \alpha_s}{\partial x} + p_{b_f} \frac{\partial b}{\partial x} - \frac{1}{\alpha_f N_R} \Bigg\{ 2\frac{\partial^2 u_f}{\partial x^2} + \frac{\partial^2 v_f}{\partial y \partial x} + \frac{\partial^2 u_f}{\partial y^2} - \frac{\chi u_f}{\varepsilon^2 h^2} \Bigg\} \\ + \frac{1}{\alpha_f N_{R_\mathcal{A}}} \Bigg\{ 2\frac{\partial}{\partial x} \Bigg(\frac{\partial \alpha_s}{\partial x} (u_f - u_s) \Bigg) + \frac{\partial}{\partial y} \Bigg(\frac{\partial \alpha_s}{\partial x} (v_f - v_s) + \frac{\partial \alpha_s}{\partial y} (u_f - u_s) \Bigg) \Bigg\} \\ - \frac{\xi \alpha_s (u_f - u_s)}{\varepsilon^2 \alpha_f N_{R_\mathcal{A}} h^2} \Bigg] \Bigg] - \frac{1}{\gamma} C_{DG} (u_f - u_s) \left| \mathbf{u}_f - \mathbf{u}_s \right|^{J-1}, \tag{2.9}$$

$$S_{y_f} = \alpha_f \Bigg[g^y - \varepsilon \Bigg[\frac{1}{2} p_{b_f} \frac{h}{\alpha_f} \frac{\partial \alpha_s}{\partial y} + p_{b_f} \frac{\partial b}{\partial y} - \frac{1}{\alpha_f N_R} \Bigg\{ 2\frac{\partial^2 v_f}{\partial y^2} + \frac{\partial^2 u_f}{\partial x \partial y} + \frac{\partial^2 v_f}{\partial x^2} - \frac{\chi v_f}{\varepsilon^2 h^2} \Bigg\} \\ + \frac{1}{\alpha_f N_{R_\mathcal{A}}} \Bigg\{ 2\frac{\partial}{\partial y} \Bigg(\frac{\partial \alpha_s}{\partial y} (v_f - v_s) \Bigg) + \frac{\partial}{\partial x} \Bigg(\frac{\partial \alpha_s}{\partial y} (u_f - u_s) + \frac{\partial \alpha_s}{\partial x} (v_f - v_s) \Bigg) \Bigg\} \\ - \frac{\xi \alpha_s (v_f - v_s)}{\varepsilon^2 \alpha_f N_{R_\mathcal{A}} h^2} \Bigg] \Bigg] - \frac{1}{\gamma} C_{DG} (v_f - v_s) \left| \mathbf{u}_f - \mathbf{u}_s \right|^{J-1}, \tag{2.10}$$

where

$$C_{DG} = \frac{\alpha_s \alpha_f (1-\gamma)}{[\varepsilon \mathcal{U}_T \{ \mathcal{P}\mathcal{F}(Re_p) + (1-\mathcal{P})\mathcal{G}(Re_p) \}]^J}, \gamma = \frac{\rho_f}{\rho_s}, \mathcal{F} = \frac{\gamma}{180} \left(\frac{\alpha_f}{\alpha_s} \right)^3 Re_p, \tag{2.11}$$

$$\mathcal{G} = \alpha_f^{M(Re_p)-1},\ Re_p = \frac{\rho_f d \mathcal{U}_T}{\eta_f}, N_R = \frac{\sqrt{gL} H \rho_f}{\alpha_f \eta_f}, N_{R_\mathcal{A}} = \frac{\sqrt{gL} H \rho_f}{\mathcal{A} \eta_f}.$$

In (2.7)-(2.11), $\varepsilon = H/L$ is the aspect ratio, where L is the typical length and H is the depth of the debris flow, the coefficient of frictional resistance to the flow of solid due to the roughness of the base is given and $\mu = \tan\delta$. $\mathcal{P} \in [0,1]$ interpolates the solid-like ($\mathcal{G}$) and fluid-like ($\mathcal{F}$) drag contributions to flow resistance in the generalized drag coefficient C_{DG}. $J = 1$ or 2 represent simple linear or quadratic drag. $\mathcal{U}_T$ represents the terminal velocity of a particle. γ is the density ratio of fluid to solid, M is a function of the particle Reynolds number (R_{e_p}), χ includes vertical shearing of fluid velocity, and ξ includes different distributions of α_s. $\mathcal{A}$ is the mobility of the fluid at the interface. N_R and $N_{R_\mathcal{A}}$ are respectively the quasi- and mobility-Reynolds number associated with the classical Newtonian and enhanced non-Newtonian fluid viscous stresses, respectively. Slope topography is given by $b = b(x,y)$. The virtual mass coefficient $\mathcal{C}$ appears in the inertial terms as the coefficients of the relative acceleration between the phases. For the details of the multi-phase virtual mass forces, one can refer to Pudasaini and Mergili [65], and Kafle et al [30].

In vectorial form the above six equations ((2.1)-(2.6)) can be written as:

$$\frac{\partial \mathbf{T}(\mathbf{w})}{\partial t} + \frac{\partial \mathbf{f}(\mathbf{w})}{\partial x} + \frac{\partial \mathbf{g}(\mathbf{w})}{\partial y} = \mathbf{s}(\mathbf{w}), \tag{2.12}$$

where, $\mathbf{w}$ denotes the vector of conservative variables h_s, h_f, $m_{x_s}(= h_s u_s)$, $m_{x_f}(= h_f u_f)$, $m_{y_s}(= h_s v_s)$ and $m_{y_f}(= h_f v_f)$. Also, $\mathbf{f}$ and $\mathbf{g}$ are the transport fluxes in the x- and y-directions, respectively, and $\mathbf{s}$ is the source term, i.e.,

$$\mathbf{T}(\mathbf{w}) = \begin{pmatrix} h_s \\ h_f \\ m_{x_s} - \gamma\mathcal{C}\Big(m_{x_f} h_s/h_f - m_{x_s}\Big) \\ m_{y_s} - \gamma\mathcal{C}\Big(m_{y_f} h_s/h_f - m_{y_s}\Big) \\ m_{x_f} + \mathcal{C}\Big(m_{x_f} h_s/h_f - m_{x_s}\Big) \\ m_{y_f} + \mathcal{C}\Big(m_{y_f} h_s/h_f - m_{y_f}\Big) \end{pmatrix}, \quad \mathbf{w} = \begin{pmatrix} h_s \\ h_f \\ m_{x_s} \\ m_{y_s} \\ m_{x_f} \\ m_{y_f} \end{pmatrix},$$

$$\mathbf{f} = \begin{pmatrix} m_{x_s} \\ m_{x_f} \\ m_{x_s}^2/h_s - \gamma\mathcal{C}\Big(m_{x_f}^2 h_s/h_f^2 - m_{x_s}^2/h_s\Big) + \beta_{x_s} h_s h/2 \\ m_{x_s} m_{y_s}/h_s - \gamma\mathcal{C}\Big(m_{x_f} m_{y_f} h_s/h_f^2 - m_{x_s} m_{y_s}/h_s\Big) \\ m_{x_f}^2/h_f + \mathcal{C}\Big(m_{x_f}^2 h_s/h_f^2 - m_{x_s}^2/h_s\Big) + \beta_{x_f} h_f h/2 \\ m_{x_f} m_{y_f}/h_f + \mathcal{C}\Big(m_{x_f} m_{y_f} h_s/h_f^2 - m_{x_s} m_{y_s}/h_s\Big) \end{pmatrix},$$

$$\mathbf{g} = \begin{pmatrix} m_{y_s} \\ m_{y_f} \\ m_{x_s} m_{y_s}/h_s - \gamma\mathcal{C}\Big(m_{x_f} m_{y_f} h_s/h_f^2 - m_{x_s} m_{y_s}/h_s\Big) \\ m_{y_s}^2/h_s - \gamma\mathcal{C}\Big(m_{x_f}^2 h_s/h_f^2 - m_{y_s}^2/h_s\Big) + \beta_{y_s} h_s h/2 \\ m_{x_f} m_{y_f}/h_f + \mathcal{C}\Big(m_{x_f} m_{y_f} h_s/h_f^2 - m_{x_s} m_{y_s}/h_f\Big) \\ m_{x_f}^2/h_f + \mathcal{C}\Big(m_{y_f}^2 h_s/h_f^2 - m_{y_s}^2/h_s\Big) + \beta_{y_f} h_f h/2 \end{pmatrix}, \quad \mathbf{s} = \begin{pmatrix} 0 \\ 0 \\ hS_{x_s} \\ hS_{y_s} \\ hS_{x_f} \\ hS_{y_f} \end{pmatrix}. \tag{2.13}$$

To numerically integrate the model Total Variation Diminishing (TVD) Non-Oscillatory Central (NOC) scheme [4, 64, 71], has been implemented here. The debris depth h, solid volume fraction α_s, velocity components for solid (u_s, v_s), and for fluid (u_f, v_f) in x- and y-directions, respectively, are computed as functions of space and time (Fig. 3.1). The model equations are solved in conservative variables $\mathbf{W} = (h_s, h_f, m_{s_x}, m_{f_x}, m_{s_y}, m_{f_y})^t$, where $h_s = \alpha_s h$, $h_f = \alpha_f h$ are the solid and fluid contributions to the debris, or the flow height; and $m_{s_x} = \alpha_s h u_s$, $m_{f_x} = \alpha_f h u_f$; $m_{s_y} = \alpha_s h v_s$, $m_{f_y} = \alpha_f h v_f$ are respectively the solid and fluid momenta in x- and y-directions.

Chapter 3

Results of Numerical Experiments and Discussion

For our simulation purpose, our three-dimensional set-up is as shown in Fig. 3.1, where a two-phase initial release mass in subaerial slope inclined at $\zeta_0 = 45°$ collapses and moves cross-slope and downslope and hits a fluid reservoir downstream. The left end of the reservoir meets an inclined surface at $x = 175$ m, where the fluid depth starts from 0 m. The inclined surface continues to $x = 200$ m, where the water height is $h = 25$ m. After this, the depth is constant (25 m) upto the right coast at $x = 300$ m, at $t = 0$ s, the

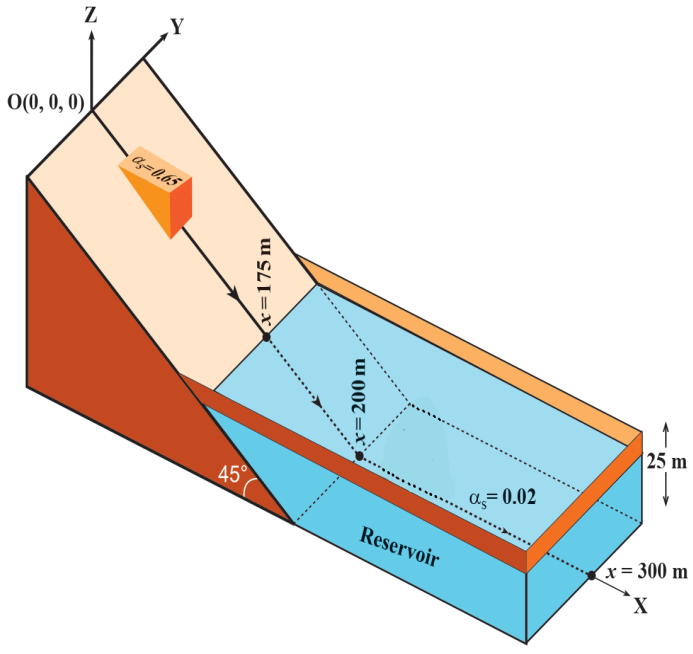

Figure 3.1: A sketch showing the initial set up with the initial release and the fluid reservoir.

release mass at the shape of laterally-spanned triangular wedge ($x_l \leq x \leq x_r$; $y_u \leq y \leq y_d$) with uniform composition of 65% solid ($\alpha_s = 0.65$) and 35% fluid ($\alpha_f = 0.35$) begin to disperse crosswise and also shears downslope. Initially, the reservoir ($175 \leq x \leq 300$ m, $-110 \leq y \leq 110$ m) consists of 2% solid and 98% fluid. The other common parameter values chosen for different simulations are: $\phi = 45°$, $\delta = 15°$, $\rho_f = 1,100$ kg m^{-3}, $\rho_s = 2,900$ kg m^{-3}, $N_R = 30,000$, $N_{R_\mathcal{A}} = 1,000$, $Re_p = 1$, $\mathcal{U}_T = 5.0$ m s^{-1}, $\mathcal{P} = 0.75$, $J = 1$, $\chi = 3$, $\xi = 5$, $\mathcal{C} = 0.5$.

We employ the aforementioned initial setup, model, parameters and numerical integration technique for our research. We simulate the two-phase landslide, resulting tsunamis and their interactions. We differ the sizes and volumes of initial release mass by extending or contracting it along down-slope or cross-slope directions. In all the simulation results presented here, the vertical dashed line in blue at $x = 170$ m indicates the left coast of the reservoir. The arrows in the top panels indicate the flow direction.

3.1 Reference Simulation

First, we discuss about reference simulation with initial release positioned at $x_l = 75 \leq x \leq x_r = 125$ m; $y_d = -25 \leq y \leq y_u = 25$ m (Fig. 3.2) that hits the fluid reservoir. This type of laterally confined boundaries, as considered here and in all the other simulations can model many natural setups.

Fig. 3.2 exhibits the reference simulation results of the timely evolution of total debris bulk, along with separate evolution of the solid and fluid phases. Initially, the maximum of the debris depth was at the front. On contrary, it has shifted towards central part at $t = 1$ s. The shearing and dispersion of the flowing mass results in the decrease of the debris depth as shown by the colour bars given alongside. At about $t = 3$ s, the flowing mass strikes at the centre of the left coast of the reservoir so as to produce tsunami that propagates in all directions. The process continues even with higher momentum ($t = 5$ s, left panel d) and the tsunami is expanded further in the vicinity of the impact ($t = 7$ s, left panel e). The displaced fluid in the reservoir produces a distinct impact vacuum. Until 9 s, the interesting phenomena to be observed are: (i) flowing debris in the subaerial slope (ii) submarine mass movement in the reservoir downstream (iii) surface tsunami. The confinements in the lateral and right coasts in the reservoir localize the tsunami near the lateral boundaries.

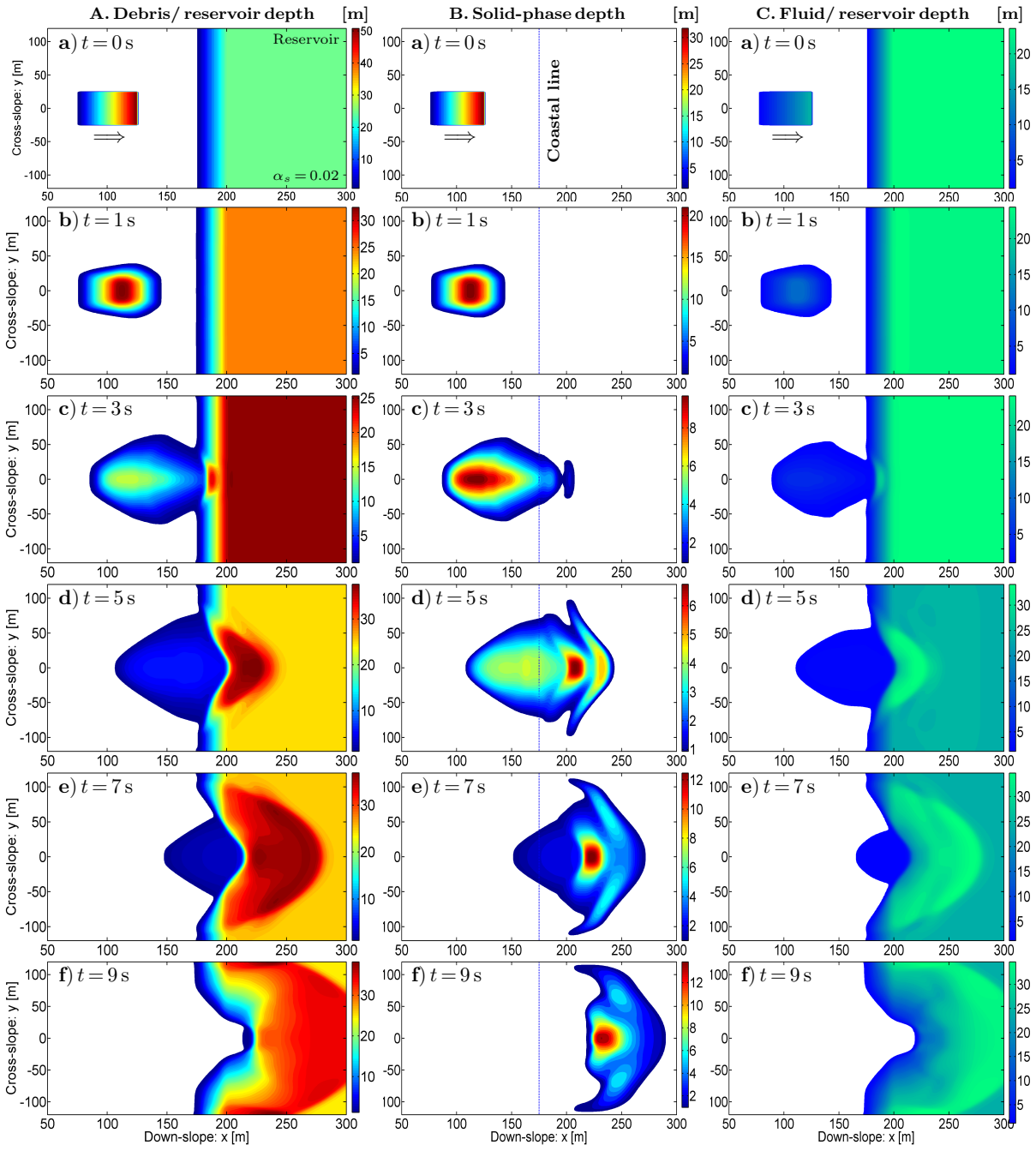

Figure 3.2: **Reference Simulation** (Base of the initial debris mass at $75 \leq x \leq 125$ m, $-25 \leq y \leq 25$ m). **A:** Total height of the debris mass and tsunami waves. Tsunami is generated, amplified and propagates as time elapses. **B:** Evolution of the solid phase in the debris mixture in subaerial part as well as in the reservoir. The solid phase advects and disperses both in subaerial slope and the bathymetry, with the formation of special solid wave. **C:** Evolution of the fluid constituent in the debris mixture and the reservoir. Tsunami amplitude in each time slice is the excess fluid height over the initial fluid height (25 m) in the reservoir [28].

The flow behavior of fluid part is seen in Fig. 3.2 C. Similar to the total debris bulk, fluid part of the debris mixture also disperses and advects as time elapses. After $t = 3$ s, the relative maxima in the right panels show how the tsunami is generated and it propagates downslope and across. We observe that the fluid-only and the total geometric evolutions are not much different as the fluid component (volume fraction) in the reservoir dominates the solid in the reservoir [31]. However, at $t = 7$ s, the geometric evolution of the total (left panel e) and the fluid-only part (right panel e) are more interesting to compare with each other. The comparison clearly reveals that the major portion of the maximum at the central part is due to the solid contribution of the debris mass and the frontal and lateral parts of the maxima arise mainly due to the evolving and propagating tsunami.

The solid-phase dynamics as shown in Fig. 3.2 B is completely different from the total and the fluid-phase dynamics, especially in the reservoir. As the mass is released at $t = 0$ s, the front is rarefied and accelerated downslope and across mainly due to the pressure gradient and gravity. As the material friction and the support of the front part are effective, the rear part of the solid body takes some more time to spread and to flow downslope. After the mass is released, the front is propagating downslope. Nevertheless, from $t = 1$ s (right panel b) to $t = 3$ s (right panel c), the solid maximum has shifted its position a bit upslope. From $t = 5$ s (right panel d) onward, the maximum height position is shifted downslope as it moves further downslope. In Fig. 3.2 B, maximum solid height has continuously decreased from 30 m at $t = 0$ s to 6 m at $t = 5$ s when it undergoes continuous shearing. But, it increases to ≥ 12 m at $t = 7$ s as it looses momentum in the run out zone. The landslide mass changes its geometrical shape mainly due to its deformation and the impact on the fluid reservoir after $t = 3$ s. From $t = 5$ s onward (right panel, d-f), it forms a very special forward propagating laterally wide and curved solid-wave.

In this reference simulation, the volume of the initial release is 62500 m^3. In the remaining simulations, we change (increase or decrease) the volume of the initial debris mass by varying its extent either along up/downslope direction (i.e., along x-axis) or cross-slope direction (i.e., along y-axis) to observe the changes in the dynamics of the tsunami and submarine mass. As we already mentioned that the geometrical evolutions of the total and the fluid part of the debris flow and the waves in the reservoir are almost similar, we do not present the fluid-only part in the remaining simulations.

3.2 Variation of volume of initial debris mass by changing its extent along x-direction

We now present and discuss some simulations by the variation of the volume of initial debris mass by changing the length of the initial debris mass along x-direction without changing its length along y-direction.

3.2.1 Reduction of volume of the initial mass

First, we reduce the volume of the initial debris mass by reducing its base area with its boundary on $[85, 115]$ m $\times[-25, 25]$ m so that the length of the initial debris mass is decreased by 20 m (Fig. 3.3) as compared to the reference simulation (Fig. 3.2). This makes the new volume of the initial debris mass $22,500$ m^3, with a reduction of 64% as compared to the reference simulation (Fig. 3.2). Fig. 3.3 presents the simulation results for the evolution of the subaerial debris flow before and submarine debris flow after the flow-reservoir-impact, and the subsequent complex fluid waves. The detailed dynamical differences in the solid and fluid waves due to the changes in volume and the positions of the front and the rear parts of the initial release mass are discussed below.

At $t = 1$ s, the debris depth increases slowly from the front to the main body due to less volume. The flowing mass is just about to hit the center of left coast of the reservoir at about $t = 3$ s. Tsunami with relatively smaller amplitude for $t \geq 5$ s (left panel, d-f) has been produced that expands slower in the vicinity of the impact ($t = 7$ s, left panel e). The area of the impact vacuum is also smaller than in Fig. 3.2. At $t = 9$ s, the frontal tsunami just begins to hit the right coast of the reservoir, whereas in Fig. 3.2, it has already hit the right coast. Due to the decreased amount of the initial debris mass, its lateral dispersion has decreased, and here the tsunami propagates less cross-slope than in Fig. 3.2.

Fig. 3.3 B presents the different flow behavior of the solid part. As the mass is released, the front is slowly rarefied and accelerating mainly due to the less pressure gradient as compared to Fig. 3.2 B. In Fig. 3.3 B, maximum solid height has continuously decreased from 20 m at $t = 0$ s to 3.5 m at $t = 5$ s by its spreading, and increased to a bit more than 5 m at $t = 7$ s. The solid phase dynamics and the deposition morphology here are both different from those in Fig. 3.2 mainly in the downslope advection, cross-slope dispersion and the positions of relative solid maxima.

In Fig. 3.3 B, the cross wise elongated frontal local maximum of solid is followed by other two centralized local maxima at $t = 5$ s and 7 s. Unlike in the previous case (Fig. 3.2),

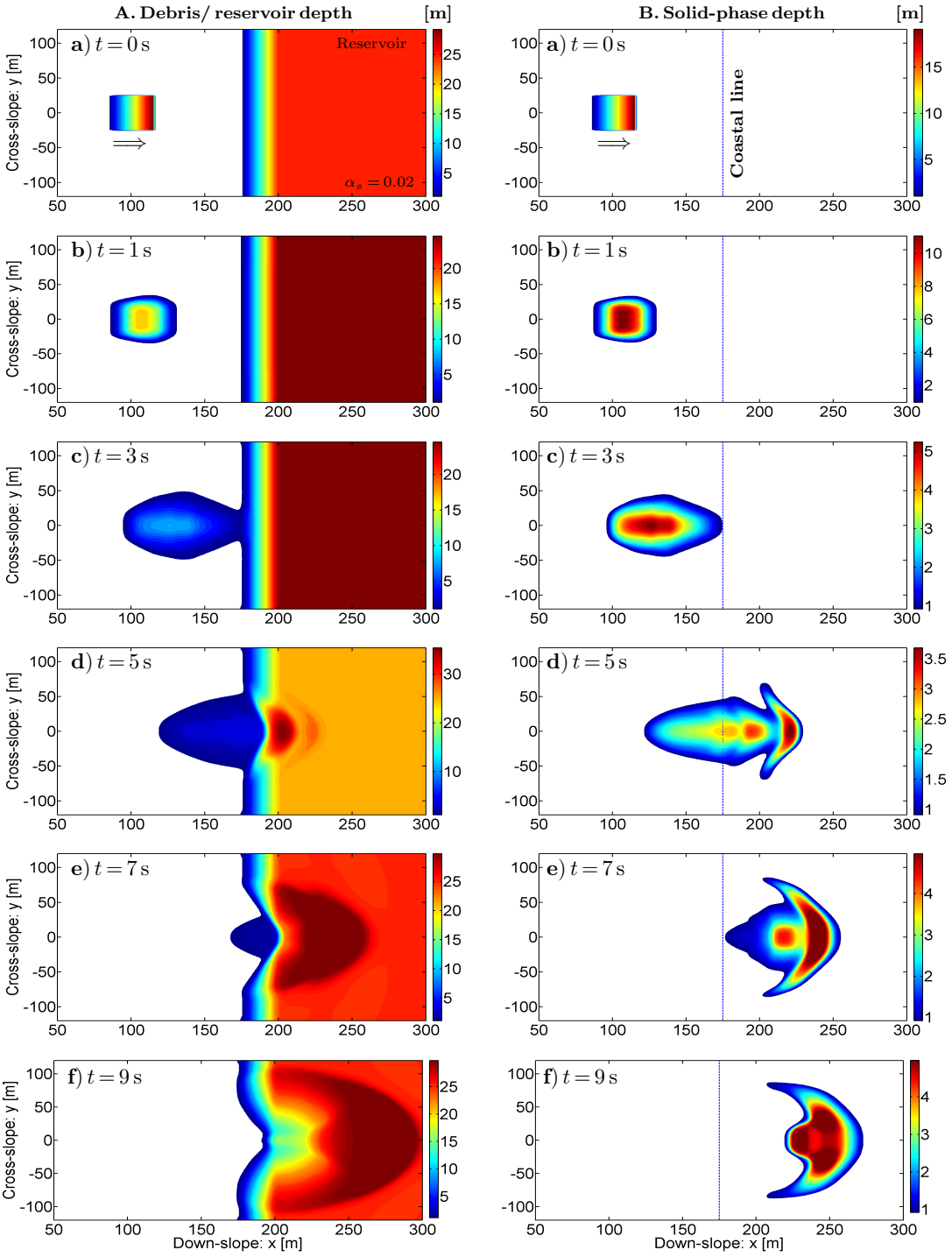

Figure 3.3: **Reduced volume of the initial debris mass** (Base of the initial debris mass at $85 \leq x \leq 115$ m, $-25 \leq y \leq 25$ m) **A:** Total height of the debris mass and tsunami waves. As time elapses, less intensified tsunami is produced that propagates less cross-slope and downslope than in Fig. 3.2. **B:** Evolution of the solid phase in the debris mixture in the subaerial as well as in the reservoir. The solid part of the debris body is less dispersed that also moves less downslope, but the solid maximum is wider than in Fig. 3.2.

the solid phase reveals three localized maxima, two weakly separated in the front, and another at a bit back of the solid body at $t = 9$ s. At $t = 7$ s, the solid debris part has just crossed the coastal line ($x = 175$ m, the beginning of the reservoir water surface). This means, the solid components enters completely into the reservoir after $t = 7$ s (right panel e), whereas a considerable amount of solid was also observed upslope of the coastal line in Fig. 3.2.

3.2.2 Increment of volume of the initial mass

Figure 3.4 presents the simulation results when the volume of the initial debris is increased by increasing the length of the base along x-axis by 20 m from the reference simulation (Fig. 3.2). Now, the new position of the base is at $65 \leq x \leq 135$ m, $-25 \leq y \leq 25$ m. By this, the volume of the initial debris will be $1,22,500$ m^3 which is 94% larger than in Fig. 3.2. All the other physical and geometrical parameters are same as the reference simulation.

Due to larger pressure gradient, the maximum debris depth quickly shifts its position the front to the main body at $t = 1$ s (Fig. 3.4 A). Since the maximum of the initial debris mass lies at its frontal part, which is nearer to the reservoir than in the previous cases, the flowing mass hits the fluid at the centre of the reservoir already at about $t = 3$ s, and the tsunami in the order of 15 m has been produced at that time. But in the previous cases (Fig. 3.2 A and Fig. 3.3 A), the amplitudes were very low or even not produced at that time. The produced tsunami with higher intensity propagates faster both cross-slope and downslope. The tsunami front reaches the right and lateral coasts earlier (already at $t = 7$ s) than the previous cases. The tsunami dynamics is even more interesting to observe at $t = 9$ s. The impact vacuum or crater is wider than the previous cases. The tsunami waves reflect after reaching the right cost and are a bit dispersed throughout the surfae of the reservoir, especially waves with higher intensity are localized in the vicinity of the lateral boundaries. This result is in line with the fact that the coastal threats increase more significantly due to the induced tsunami by the landslide or debris flow with larger volume.

The solid phase dynamics as shown in Fig. 3.4 is also significantly different from those in Fig. 3.2, and the difference is more pronounced as time elapses. In Fig. 3.4 B, maximum solid height continuously decreases from 40 m at $t = 0$ s to 12 m at $t = 5$ s by its spreading, and increased to a bit more than 14 m at $t = 7$ s and 20 m at $t = 9$ s. But after $t = 5$ s (right panel d), it increases because the solid tends to halt as it looses momentum at the horizontal bathymetry. After $t = 3$ s, due to the impact of the flowing

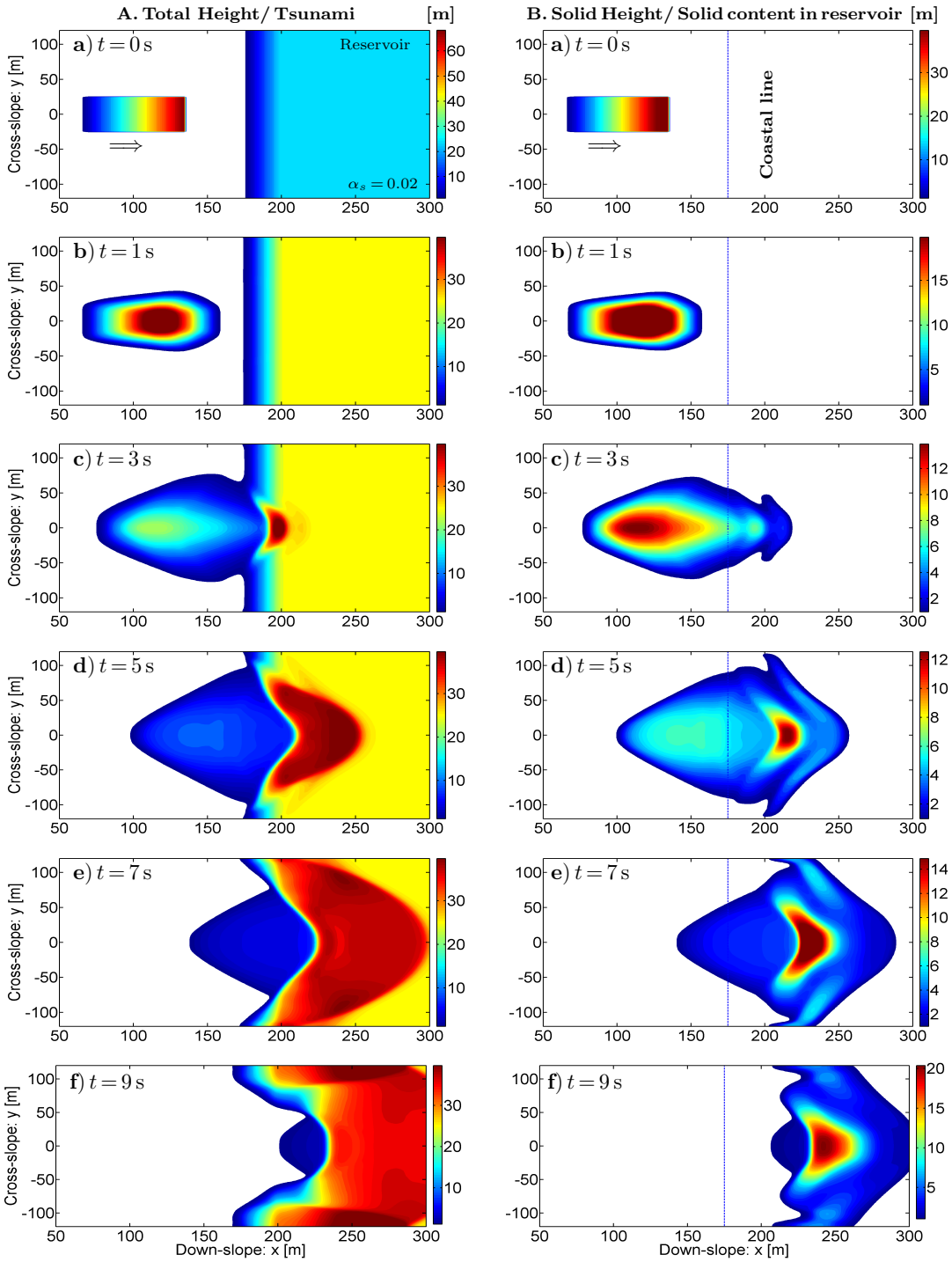

Figure 3.4: **Increased volume of initial debris mass** (Base of the initial debris mass at $65 \leq x \leq 135$ m, $-25 \leq y \leq 25$ m) **A:** Total height of the debris mass and tsunami waves. As time elapses, more intensified tsunami is produced that propagates more cross-slope and downslope than in Fig. 3.2 **B:** Evolution of the solid phase. In this case, the submarine mass reaches the right coast faster (already at $t = 7$ s) than in Fig. 3.2.

mass on the reservoir, the solid mass is sheared further and is elongated cross wise from the front to the middle portion ($t = 5$ s right panel d). At $t = 7$ s, the solid debris part has just about to cross the coastal line ($x = 175$ m, the beginning of the reservoir water surface). At $t = 9$ s, the fronts of solid mass were at $x = 275$ m and $x = 290$ m in Fig. 3.3 and Fig. 3.2, whereas in Fig. 3.4, it already hits the right coast of the reservoir. This is so because larger volume of initial debris mass accelerates more than the case of less volume, especially due to the larger pressure gradient. We observe completely different dynamics and depositional behaviour of the submarine mass for the different volumes of the initial release mass. The results support that it might be dangerous to make civil structures around the banks of the water bodies surrounded by mountain flanks that contain potentially larger volume of the landslide materials that potentially undergoes destabilization.

3.3 Variation of volume of initial debris mass by changing its extent along y-direction

In this section, we present and discuss some simulations by changing the volume of initial debris mass by varying the length of the initial debris mass along y-direction without changing its length along x-direction.

3.3.1 Reduction of volume of the initial debris mass

Here, we simulate with the decreased volume of initial debris mass ($75 \leq x \leq 125$ m, $-15 \leq y \leq 15$ m) by decreasing cross-slope length of the initial debris mass by 20 m (Fig. 3.5) as compared to reference simulation (Fig. 3.2). This makes the volume of the initial debris mass $37,500$ m^3, with a reduction in volume by 40% of the reference simulation.

At $t = 1$ s, the height of the flowing mixture increases rapidly (as in Fig. 3.2) from its front to its main body as the length of the debris mass has been reduced along the cross slope direction. The flowing mass already hits the centre of the left coast of the reservoir at about $t = 3$ s. After that, tsunami with smaller amplitude than in Fig. 3.2 is produced that propagates further for $t \geq 5$ s (left panel d onward). At $t = 5$ s, increased height of the fluid surface as shown by colour bars indicates that behind the impact region, tsunami of amplitude 5 m is pushing the water to the right (up to a bit more than $x = 230$ m). In this simulation, the area of the impact vacuum is smaller than in Fig. 3.2. At $t = 9$ s, the debris mass totally enters into the reservoir, but in Fig. 3.2, a considerable amount of

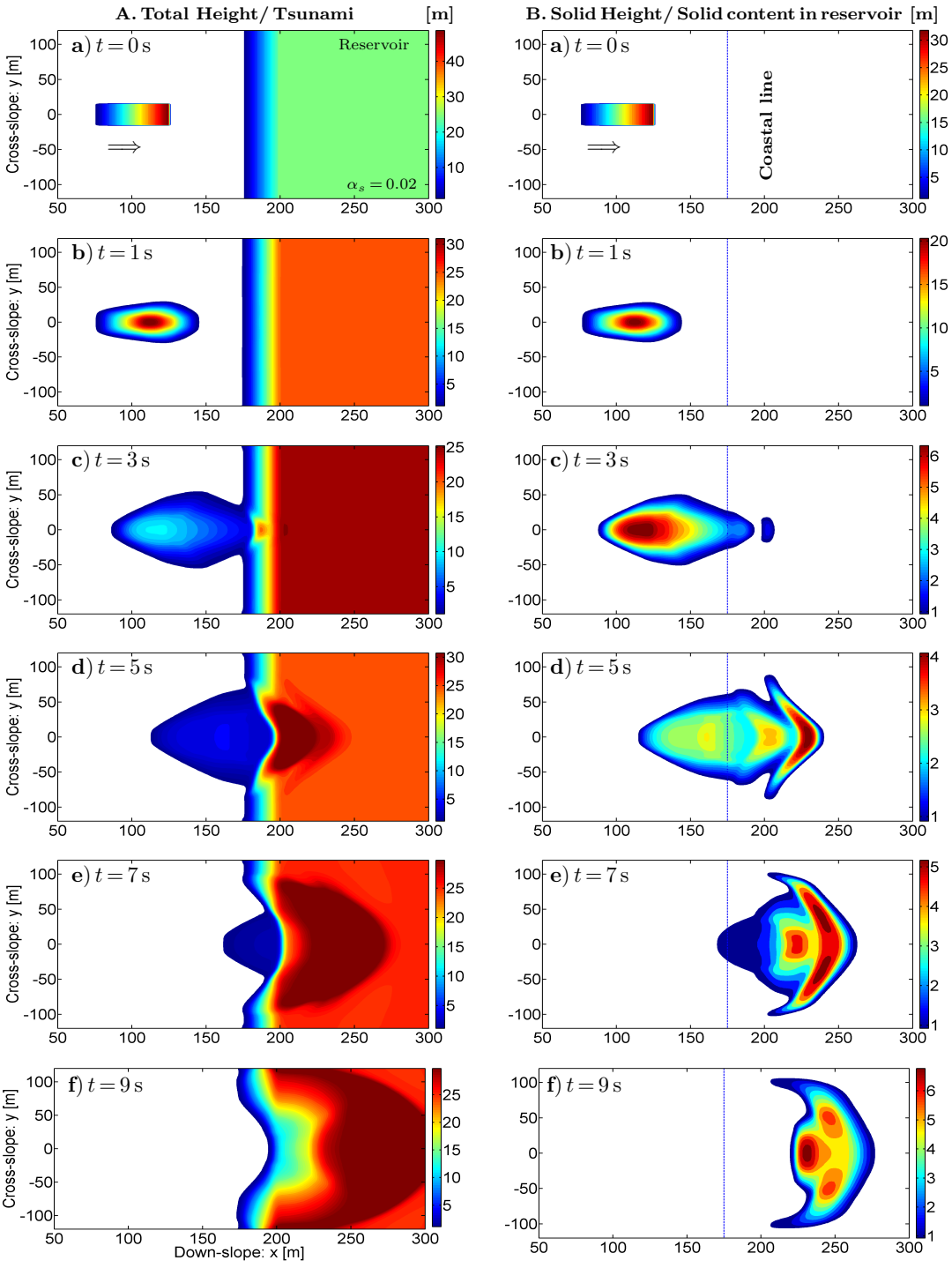

Figure 3.5: **Reduced volume of initial debris mass along cross-slope direction** (Base of the initial debris mass at $75 \leq x \leq 125$ m, $-15 \leq y \leq 15$ m) **A:** Total height of the debris mass and tsunami waves. As time elapses, less intensified tsunami is produced that propagates less cross-slope and down slope than in Fig. 3.2. **B:** Evolution of the solid phase in the subaerial slope and in the reservoir. The flowing mass attains less velocity than in Fig. 3.2.

debris mass was still outside the reservoir.

The dynamics of the solid part as seen in Fig. 3.5 B is different from the previous simulation mainly at $t = 5$ s to $t = 9$ s, where the solid maxima lie on the frontal head. At $t = 7$ s, there are three localized maxima, two weakly separated at the front and one at a bit back, whereas at $t = 9$ s, the frontal solid maxima are more separated than at $t = 7$ s.

3.3.2 Increment of volume of the initial debris mass

Now, we increase the volume of the initial debris mass by increasing its base area with its boundary on $[75, 125]$ m $\times[-35, 35]$ m so that the breadth of the initial debris mass is increased by 20 m (Fig. 3.6) as compared to the reference simulation (Fig. 3.2). This makes the volume of the debris mass $87,500$ m^3, which is 40% higher than in Fig. 3.2. Now, we present the detailed dynamical differences in the solid and fluid waves due to the changes in volume and the positions of the front and the rear part of the initial debris mass.

Since the volume of the debris mass is increased, it results in the increased debris mass that causes the debris height to increase quickly from the front to the main body at $t = 1$ s (Fig. 3.6 A). As there is larger pressure gradient at the front of the release mass, it already hits fluid reservoir at $t = 3$ s. In later times, tsunami has become more distinct and dispersed all over the surface of the reservoir. At time $t = 7$ s, the front of debris mass is at around 270 m, 280 m, 290 m in Fig. 3.5, Fig. 3.2, Fig. 3.6 respectively. This shows that debris mass is more mobile, when we increase the volume of the initial debris mass from along the cross-slope direction as well.

The dynamics of the solid part in subaerial as well as the submarine part has been presented in Fig. 3.6 B, where the maximum of the solid component has continuously decreased from 30 m at $t = 0$ s to 10 m at $t = 5$ s by its spreading, and increased to a bit more than 15 m at $t = 7$ s, and 20 m at $t = 9$ s. The solid dispersion has also increased from $t = 5$ s (right panel d) to $t = 9$ s (right panel f). At $t = 9$ s, the front of solid mass is at $x = 275$ m, $x = 290$ m, and $x = 300$ m in Fig. 3.5 B, Fig. 3.2 B, Fig. 3.6 B respectively. As the volume is increased from along the cross-slope, the submarine mass also moves faster along downslope. This seems to be counter intuitive. However, this can be explained. In fact, the pressure gradient of the initial release mass increases its mobility.

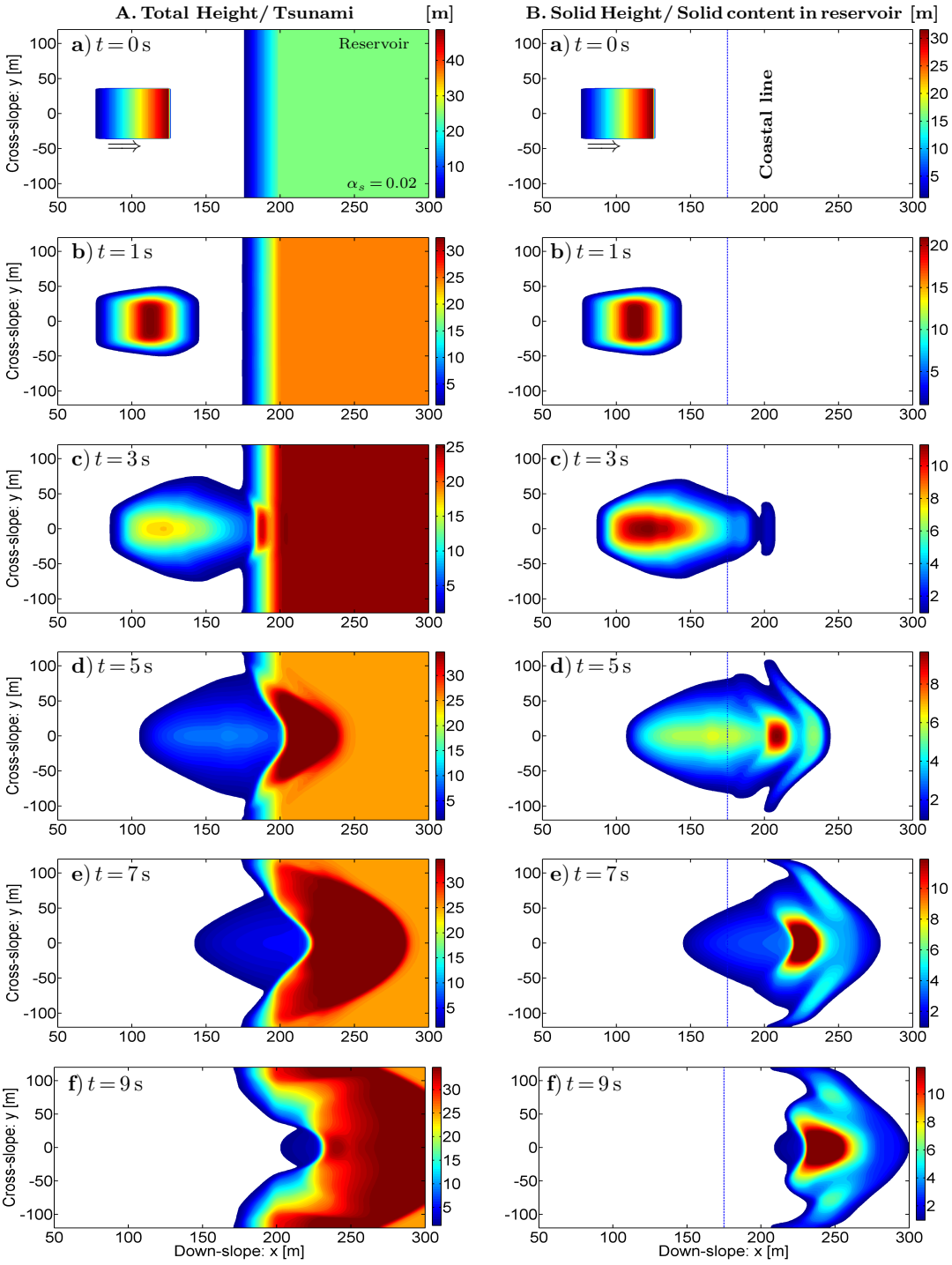

Figure 3.6: **Increased volume of initial debris mass along Cross-slope direction** (Sase of the initail debris mass at $75 \leq x \leq 125$ m, $-35 \leq y \leq 35$ m) **A:** Total height of the debris mass and tsunami waves. As time elapses, a bit more intensified tsunami wave is produced that propagates more cross-slope and downslope then in Fig. 3.2. **B:** Evolution of the solid phase in the debris mixture. In this case, the submarine mass just starts hitting the right coast of the reservoir at $t = 9$ s, whereas in Fig. 3.2 it was more upslope of right coast of the reservoir.

3.4 Variation of volume of initial release mass by reducing its extent along both x- and y- directions

First, we reduce the volume of the initial debris mass by restricting its base area within the boundary on $[85, 115]$ m and $[-15, 15]$ m so that the extent of the base decreases from both $x-$ and $y-$ directions. This reduction of base along downslope and cross-slope results the reduction of 78.4% of the original mass that we considered in the reference simulation (Fig. 3.2). The evolution of the subaerial debris flow, submarine mass flow after the flow-reservoir impact and the subsequent complex fluid waves are presented here in Fig. 3.7 and their comprehensive dynamical differences are discussed.

At $t = 1$ s, the debris depth, and maximum depth position alters its position from the front to the main body. The debris is just about to hit the centre of left shore of the reservoir at about $t = 3$ s. As the debris hits and penetrates the reservoir, the impacting mass generates tsunami with relatively smaller amplitude for $t \geq 5$ s (left column, d-f) as compared to the reference simulation Fig. 3.2. This is because less flowing mass causes sudden decrease in the momentum. This physical scenario is clearly illustrated in the simulation. The tsunami has been expanded slowly in the vicinity of the impact ($t = 7$ s, left panel e) and fluid mass from the left of the reservoir is pushed forward and laterally during the flow. At $t = 5$ s, the level of the water surface has increased to 30 m at around $x = 240$ m due to the tsunami generation on impact. The colour map shows that the tsunami propagates in all directions. The area of the impact vacuum and tsunami propagation are also comparatively smaller than those in Fig. 3.2.

The dynamics of the solid component is presented in Fig. 3.7 B as derived from the total debris from Fig. 3.7 A. As the mass is released, the front is slowly rarefied and accelerating mostly due to the lower pressure gradient relative to that in Fig. 3.2 B. In Fig. 3.7 B, maximum solid height has continuously decreased from 20 m at $t = 0$ s to nearly 3 m at $t = 5$ s through its spreading. But after $t = 5$ s, the solid halting process eventually leads to the gradual rise in the solid height to almost 7 m. The solid phase dynamics and the deposition morphology here are both different from those in Fig. 3.2 mainly in the downslope advection, cross-slope dispersion, and the positions of relative solid maxima. The debris mass fully submerges into the reservoir at $t = 7$ s. on contrary, a considerable amount of solid was upslope of the coastal line in Fig 3.2. This indicates the lower mobility of the debris mass by the reduction in volume of original debris mass.

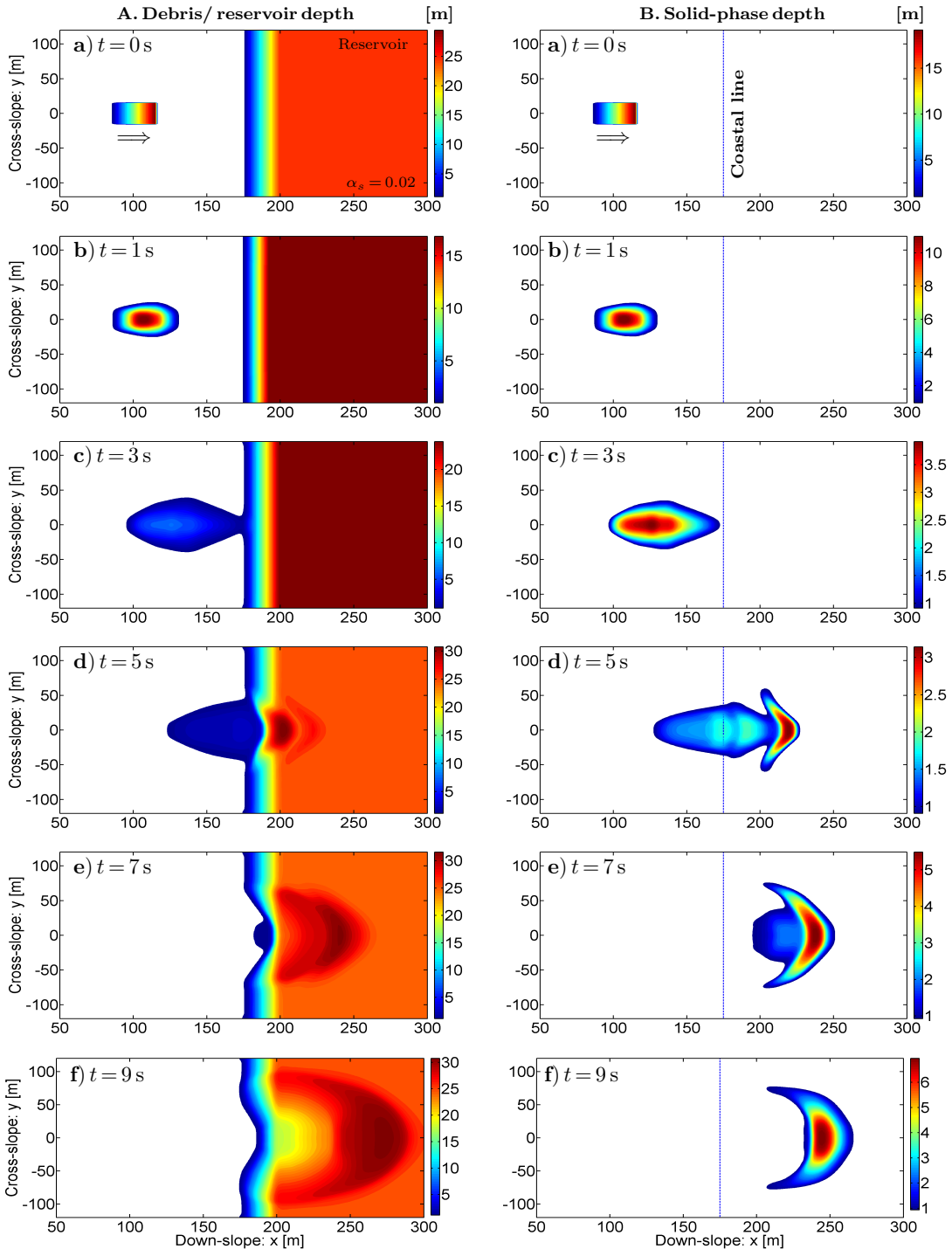

Figure 3.7: **Reduced volume of the initial debris mass** (Base of the initial debris mass at $85 \leq x \leq 115$ m, $-15 \leq y \leq 15$ m) **A:** Total height of the debris mass and tsunami waves. As time elapses, less intensified tsunami is produced that propagates less cross-slope and downslope than in Fig. 3.2. **B:** Evolution of the solid phase. The solid part of the debris body is less dispersed that also moves less downslope.

3.5 Variation of volume of initial debris mass by increasing its extent along both x- and y-directions

Now, we increase the volume of the original initial debris mass by extending its base area both along x- and y-directions so that the the base of the initial release is within the boundary on $65 \leq x \leq 135$ m and $-35 \leq y \leq 35$ m. This expansion massively increases the volume of the release to 171,500 m^3 which becomes 2.744 times bigger than the original release mass in the reference simulation Fig. 3.2. Figure 3.8 presents the simulation results to study the effect of change in volume of initial debris mass as mentioned above and without changing other physical and geometrical parameters from the reference simulation.

Then, we analyze the dynamic variations of both solid and fluid in different simulations. The effect of this remarkable increment of the volume of initial release can be seen instantly at $t = 1$ as the debris maxima quickly shifts from front to the main body due to gravity and the relatively higher pressure gradient (Fig. 3.8 A). As a result, the sliding mass strongly hits the centre of left shore promptly at $t = 3$ s and the height of the water surface has substantially increased at $t = 5$ s producing strong water waves. At time $t = 7$ s, the front of debris mass has moved forward to near about right coast but it was around at 275 m, and 250 m respectively in Fig. 3.2, and Fig. 3.7 respectively. This indicates the greater mobility of the mass when its volume is relatively increased by elongating the mass along both the cross-slope and down-slope directions.

The flow behavior of the solid part is presented in Fig. 3.8 B, where the maximum solid height is continuously decreasing from 30 m at $t = 0$ s to 17 m at $t = 5$ s by its ongoing spreading and then it begins to scale up. In fact, greater volume of initial mass ultimately deposits to a larger extent with more solid height. This is evident in Fig. 3.8B as the maxima of the solid component finally increases to nearly 25 m at $t = 9$ s due to the mass deposition process but it was only about 13 m and 7 m in Fig. 3.2, Fig. 3.7 respectively when the initial release volumes were relatively smaller. The faster lateral spreading of the solid mass can be observed from $t = 5$ s (right panel d) to $t = 9$ s (right panel f) as the mass strongly hits the right coast but it hardly crossed the mid of reservoir in previous simulations.

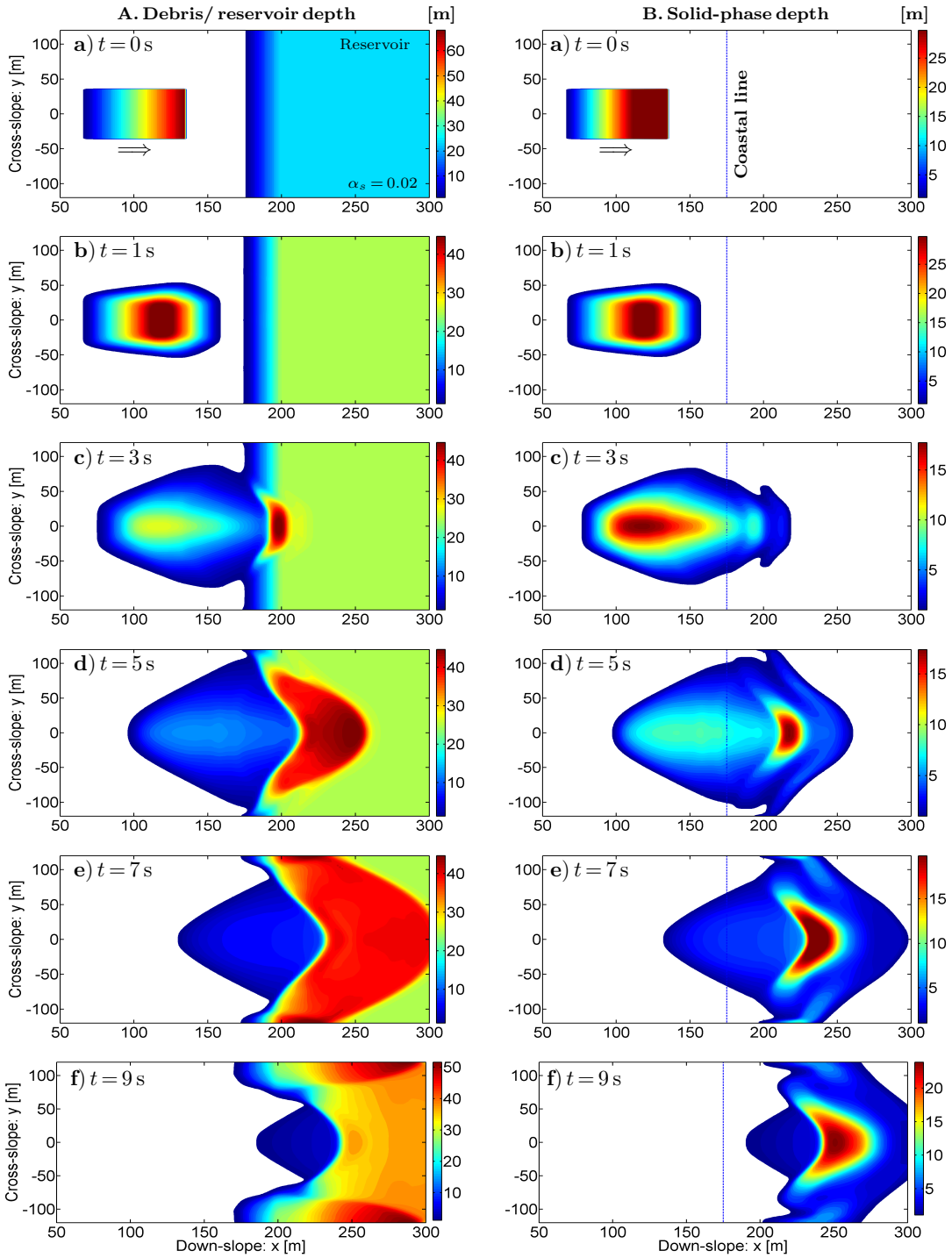

Figure 3.8: **Increaded volume of the initial debris mass** (Base of the initial debris mass at $65 \leq x \leq 135$ m, $-35 \leq y \leq 35$ m) **A:** Total height of the debris mass and tsunami waves. As time elapses, more intensified tsunami is produced that propagates more cross-slope and downslope than in Fig. 3.2. **B:** Evolution of the solid phase in the debris mixture. In this case, the submarine mass reaches the right coast faster than in Fig. 3.2 (already at t = 7 s).

3.6 Comparisons of tsunami amplitudes and run-out scenarios

Now, we discuss the change in tsunami amplitudes and run-out scenarios of the different results in different simulations. As high-intensity tsunamis are observed in t = 7 s in almost all cases, we compare the amplitudes (A_i) of the tsunamis at this time (see Table 3.1).

In the reference simulation when the base of the initial debris mass is at $75 \leq x \leq 125$ m; $-25 \leq y \leq 25$ m, the highest tsunami amplitude (at around x = 250 m) was of $A_0 = 12$ m. When the volume of initial release is increased by extending its base along the down-slope, and both of down-slope and cross-slope, then the tsunami amplitude also increases i.e., $A_0 < A_2, A_6$. When the volume was increased through the cross-slope, and the volume is decreased, the tsunami amplitude is decreased, i.e., $A_0 > A_1, A_3, A_4, A_5$ (See, Table 3.1). When the cross-slope length of the release mass is increased keeping downslope length constant, then the tsunami amplitude is decreased by nearly $(((12 - 10)/12) \times 100) = 16.66\%$. With this result, we can conclude that the surface area that hits the reservoir affects the tsunami amplitude. In fact, when we increase the volume by increasing its base area along the down-slope direction, the flow with higher momentum and kinetic energy is produced that resulted in the higher tsunami intensity. And in the cases of

Table 3.1: Comparison of tsunami amplitudes in case of different volume of initial release mass at time t = 7 s.

Release mass			Tsunami amplitude	
Simulation type	index: i	Volume [m^3]	A_i [m]	$\frac{A_i}{A_0}$
Reference simulation	0	62500	12(= A_0)	1
Contracting base area along downslope	1	22500	5	0.4167
Extending base area along downslope	2	122500	15	1.25
Contracting base area along cross-slope	3	37500	4	0.333
Extending base area along cross-slope	4	87500	10	0.833
Contracting base area both ways	5	13500	6	0.5
Extending base area both ways	6	171500	19	1.1667

decreased volume as compared to the reference simulation, we observe that the tsunami amplitude is also decreased. If we look at the volume perspective, we see that $V_2 < V_6$ but $A_2 > A_6$ that means larger the volume of the release mass does not always result in larger amplitude. In fact, it depends in which way the volume is increased.

It is interesting to compare the maximum solid height of the debris mass at time t= 9 s. Table 3.2 presents the detailed quantitative description of the maximum solid depth and their comparisons with the reference simulation ($75 \leq x \leq 125$ m, $-25 \leq y \leq 25$ m). In the reference simulation, the maximum solid mass gets accumulated at the central part of the reservoir. When the initial release volume is decreased by restricting its base area through down-slope, cross-slope or both of them, then from table 3.2, we see that the maximum solid height also decreases i.e., $M_2, M_4, M_6 < M_0$. In the same way, if the volume is increased, we see that the maximum solid height at $t = 9$ s also increases, i.e., $M_3, M_5, M_7 > M_0$. From this we conclude that when we increase the volume of the initial debris mass, the maximum solid height in the bathymetry also increases and vice versa.

Table 3.2: Comparison of maximum solid height in case of different volume of initial debris configurations at time t = 9 s

Obstacles configurations			Maximum solid height	
Simulation type	index: i	Volume [m^3]	M_i [m]	$\frac{M_i}{M_0}$
Reference simulation	1	62500	14(= M_0)	1
Contracting base area along downslope	2	22500	5	0.3571
Extending base area along downslope	3	122500	20	1.4286
Contracting base area along cross-slope	4	37500	6.5	0.4643
Extending base area along cross-slope	5	87500	18	1.286
Contracting base area both ways	6	13500	7	0.5
Extending base area both ways	7	171500	24	1.7143

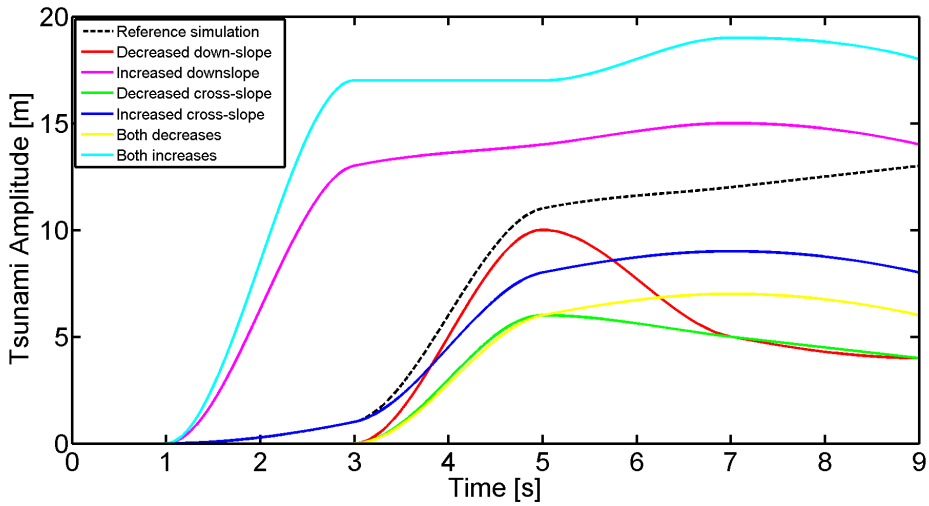

Figure 3.9: **Comparison of tsunami amplitudes.**

3.7 Comparisons of Solid front position, Position of Maximum solid heights and Tsunami Amplitudes

Now, we compare the time evolution of the tsunami amplitudes, front positions of the solid phase and the solid maximum height position in the different simulations presented over here. In the reference simulation when the base of the initial debris mass at $75 \leq x \leq 125$ m, $-25 \leq y \leq 25$ m, the highest tsunami amplitudes are of approximately 12 m (at around $x = 250$ m) and 13 m (at around $x = 300$ m) at time $t = 7$ s and $t = 9$ s respectively. In case when the release volume is increased by increasing the base area along

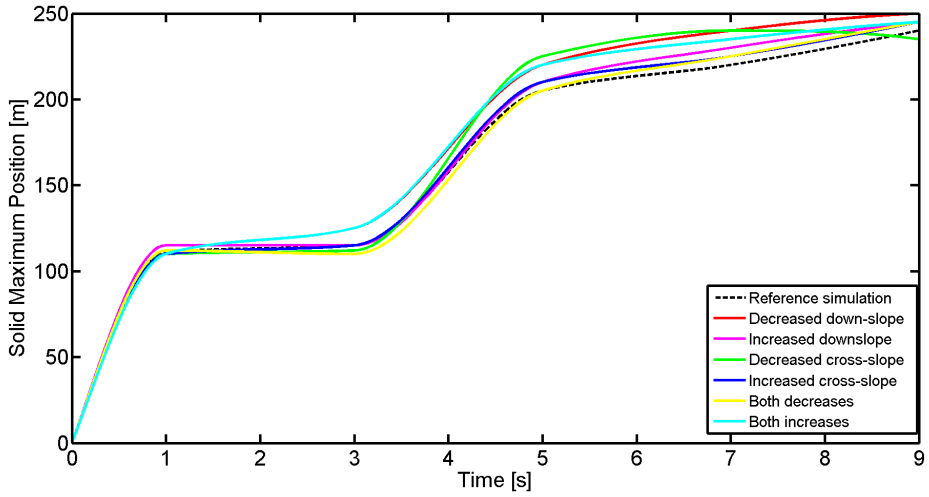

Figure 3.10: **Comparison of solid maximum positions for different volumes at $t = 0$ s to $t = 9$ s.**

down-slope and both of down-slope and cross-slope, we see that the amplitudes of tsunami waves also increase continuously. On contrary, when we increase the cross-slope length of the base area by keeping down-slope same as the reference simulation, the amplitude of the tsunami waves is decreasing and decreased by 5 m at $t = 9$ s (Fig. 3.9). When the the release volume is decreased by decreasing the lenght of the base area along down-slope, we find that the amplitude of the tsunami waves increases rapidly in between $t = 3$ s to $t = 5$ s, and then decreases by a bit then after.

Comparison of the solid maximum positions for different volumes is also very interesting to observe. In all the simulations, we see that the profile for the front positions reveal almost similar structure from the initiation to the run out. It is even more interesting from $t = 1$ s to $t = 3$ s when the maximum height of the solid is found to be almost constant (120 m). After that, the positions of maximum height of the solid again increase rapidly in all cases and reached around 210 m at $t = 5$ s. After $t = 5$ s, the position of maximum height of the solid increases slowly and reached around 250 m at 9 s.

These results and analyses show that tsunami amplitudes and runout extents are rapidly increased when the volume is enlarged by increasing the base area of the release mass in both directions. In this case, there is danger of the possible dam break downstream, threatening downstream coastal population and infrastructures. Moreover, runout extent is rapidly decreased when the volume is decreased by decreasing the base area of the release mass in both directions. In this case, the mobility of tsunami are substantially decreased by reducing the destructive wave impact, runup and the resulting damages.

Now, Fig 3.11 presents the comparison of solid front positions for the different configu-

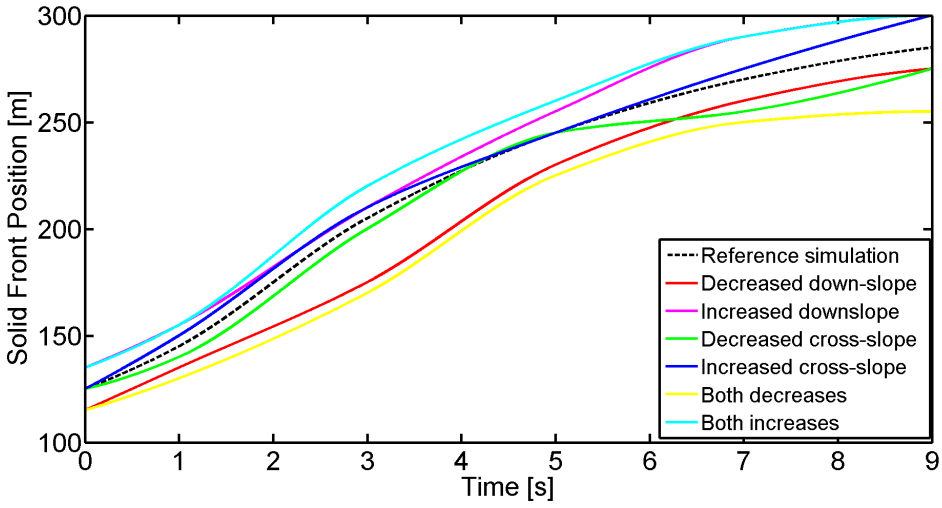

Figure 3.11: **Comparison of solid front positions for different volumes at $t = 0$ to $t = 9$ s.**

rations. Initially, for all the simulations, the front position is in between $x = 115$ m to $x = 135$ m. As the flow is triggered, it moves downslope. In due course of the flow, due to different volumes of the initial debris mass, the solid maxima evolve differently and lie at different downslope and cross-slope positions at the sliding plane and the reservoir. On comparing the solid front positions, they move downslope along with the time elapses. As the volume increases, the solid front accelerates more due to the increased gravity and so it reaches farther downslope (nearly above 300 m in the cases of increased volume) at t =9 s. In the case of decreased cross-slope it looks the solid front position is same as reference simulation at $t = 5$ s but after $t = 5$ s the acceleration decreases slowly as compared to the reference simulation.

Chapter 4

SUMMARY

A traveling mass of loose mud, soil, air, water and sand that moves down a slope under the effect of gravity is considered as debris flow. Tsunamis are long water waves which is caused by a sudden disturbance of the floor or surface of ocean, bays, sea or lakes, fjords, hydraulic reservoirs or mountain lakes and landslide dams which is generally caused by sea floor deformation, landslides, earthquakes, volcanic eruptions, slumps, shore instabilities, subsidence, meteorite, asteroid impacts and underwater explosions and landslides. The inspection and cognizance of tsunami intensity, propagation and the submarine mass movement is applicable for the hazard mitigation in the tsunami-prone zones.

The dimension (or volume) of the initial debris plays supreme roles in the degree or intensity of splash on flow-reservoir-impact, wave amplitudes and propagation speeds of the evolve water waves and possible dam breaching or over spilling of water. The increased volume of the landslide from along both down-slope and across makes the tsunami and the submarine mass more mobile adding on the risks towards the right and lateral coasts of the lakes. It has been observed that it is not only volume of the release but also the surface area of the release that impacts the reservoir also plays important role for the tsunami intensity. These results can be further elongate to analyze the required strength of the dams or embankments in response to the fluctuation of the water level due to the landslides impact. The results also justify that the degree of devastation and risks towards the natural or artificial dam of the reservoir, caused by landslide induced tsunami firmly depends on the initial volume of the release mass. Such study of landslide induced tsunami and submarine sediment transport has the significant applications in hazard mitigation, sedimentology, submarine geo-dynamics, construction of irrigation tunnels, installation of hydroelectric power plants and oil platforms and safety aspects to preserve coastal and mountain population and infrastructures.

Submitted paper

1. J. Kafle, G. Acharya, P. Kattel and P.R. Pokhrel (2021) Impact of Variation of Size of the Initial Release Mass in the Dynamics of Landslide Generated Tsunami.

2. J. Kafle, B. K. Thakur and G. Acharya (2021) Formulative Visualization of Numerical Methods for Solving Non-linear Ordinary Differential Equations.

Presentations

1. G. Acharya (2020) *Impact of Variation of Size of the Initial Debris Mass in the Dynamics of Landslide Generated Tsunami,* Seminar Cum Workshop on Mathematics and its Applications, August 29 - 30.

2. G. Acharya, P. Kattel, P.R. Pokhrel and J. Kafle (2021) *Mathematical Modeling of Landslide Generated Tsunami* International Conference on Analysis and its Applications - 2021 (ICAA_NEPAL_2021) April 9 - 11.

REFERENCES

[1] https://link.springer.com/chapter/10.1007/978-3-319-59469-9_3.

[2] https://www.ctic.ioc-unesco.org/faq-main/131-what-types-of-tsunamis-exist.

[3] R.A. Bagnold. Experiments on a gravity-free dispersion of large solid particles in a Newtonian fluid under shear. *Proc R Soc Lond, A*, 225:49–63, 1954. doi:10.1098/rspa.1954.0186.

[4] B. Domnik, S.P. Pudasaini, R. Katzenbach, and S.A. Miller. Coupling of full two-dimensional and depth-averaged models for granular flows. *J. Non-Newtonian Fluid Mech.*, 201:56–68, 2013.

[5] S. Douglas. *Numerical modeling of extreme hydrodynamic loading and pneumatic long wave generation: application of a multiphase fluid model*. Ph. D. Dissertation, University of Ottawa, Canada, 2016.

[6] F.M. Evers, V. Heller, H. Fuchs, W.H. Harger, and R.M. Boes. Landslide generated impulse waves in reservoirs - basics and computation. *2nd edition, Zurich*, 2019.

[7] E.D. Fernandez-Nieto, F. Bouchut, D. Bresch, M.J. Castro Diaz, and A. Mangeney. A new Savage-Hutter type model for submarine avalanches and generated tsunami. *J. Comput. Phys.*, 227(16):7720–7754, 2008.

[8] A. Franci, M. Cremonesi, U. Perego, E. Oate, and G. Crosta. 3d simulation of vajont disaster. part 2: Multi-failure scenarios. *Engineering Geology*, 279:105856, 2020.

[9] H.M. Fritz. *Initial Phase of Landslide Generated Impulse Waves*. PhD. Dissertation, Swiss Federal Institute of Technology, ETH Zrich, Switzerland, 2002.

[10] H.M. Fritz, W.H. Hager, and H.E. Minor. Lituya bay case: Rockslide impact and wave run-up. *Science of Tsunami Hazards*, 19:3–22, 2001.

[11] J.M.N.T. Gray. Granular flow in partially filled slowly rotating drums. *J. Fluid. Mech.*, 441:1–29, 2001.

[12] J.M.N.T. Gray, M. Wieland, and K. Hutter. Gravity-driven free surface flow of granular avalanches over complex basal topography. *Proc. R. Soc. A*, 455:1841–1874, 1999.

[13] R. Greve and K. Hutter. Motion of a granual avalanche in a convex and concave curved chute: Experiments and theoretical predictions. *Phil. Trans. R. Soc. A*, 342:573–600, 1993.

[14] S.T. Grilli, M. Ioualalen, J. Asavanant, F. Shi, J. Kirby, and P. Watts. Source constraints and model simulation of the December 26, 2004, Indian Ocean tsunami. *J. Waterw. Port Coast. Ocean Eng.*, 133:414–428, 2007.

[15] M.A. Hampton, H.J. Lee, and J. Locat. Submarine landslides. *Rev. Geophys.*, 34:33–59, 1996.

[16] W.G. Von Hardenberg. Expecting disaster: The 1963 landslide of the Vajont dam. *Environment and Society Portal, Arcadia 2011*, 8, 2011.

[17] K.B. Haugen, F. Lovholt, and C.B. Harbitz. Fundamental mechanisms for tsunami generation by submarine mass flows in idealised geometries. *Mar. Pet. Geol.*, 22(1-2):209–217, 2005.

[18] R. Hermanns, L' Heureux, J. Sebastien, and L. Blikra. Landslide triggered tsunami, displacement wave. 2013.

[19] L. Highland, S.D. Ellen, S.B. Christian, and W.M. Brown III. Debris-flow hazards in the united states, 1997. doi = 10.3133/fs17697.

[20] O. Hungr. A model for the runout analysis of rapid flow slides, debris flows, and avalanches. *Canadian Geotech. J.*, 32:610–623, 1995.

[21] K. Hutter, B. Svendsen, and D. Rickenmann. Debris flow modelling review. *Continuum Mech. Thermodyn.*, 8:1–35, 1996.

[22] R.M. Iverson. The physics of debris flows. *Rev. Geo-phys.*, 35(3):245–296, 1997.

[23] R.M. Iverson and R.P. Denlinger. Flow of variably fluidized granular masses across three-dimensional terrain: 1. coulomb mixture theory. *J. Geophys. Res.*, 106(B1):537–552, 2001.

[24] L. Innes John. Debris flows. *Progress in Physical Geography: Earth and Environment*, 7(4):469–501, 1983. doi = 10.1177/030913338300700401.

[25] J. Kafle. *Dynamic Interaction Between a Two-phase Submarine Landslide and a Fluid Reservoir*. MPhil Dissertation, Kathmandu University, School of Science, Kavre, Dhulikhel, Nepal, 2014.

[26] J. Kafle. *Advanced Dynamic Simulations of Landslide Generated Tsunami, Submarine Mass Movement and Obstacle Interaction*. PhD Dissertation, Department of Mathematics, School of Science, Kathmandu University, Kavre, Dhulikhel, Nepal, 2019.

[27] J. Kafle and P. Kattel. Simulations for rotational symmetry through r.avaflow in the general two-phase mass flow model. *Journal of Nepal Mathematical Society*, 2(2):45–60, 2019.

[28] J. Kafle, P. Kattel, M. Mergili, J.-T. Fischer, and S.P. Pudasaini. Dynamic response of submarine obstacles to two-phase landslide and tsunami impact on reservoirs. *Acta Mechanica*, 230(9):3143–3169, 2019. doi : 10.1007/s00707-019-02457-0.

[29] J. Kafle, P. Kattel, P. R. Pokhrel, K. B. Khattri, D. B. Gurung, and S. P. Pudasaini. Dynamic interaction between a two-phase submarine landslide and a fluid reservoir. *Int. J. Lsld. Env.*, 1(1):35–36, 2013.

[30] J. Kafle, P. Kattel, P.R. Pokhrel, and K.B. Khattri. Numerical experiments on effect of topographical slope changes in the dynamics of landslide generated water waves and submarine mass flows. *Journal of Applied Fluid Mechanics (JAFM)*, 4(3):61–876, 2021. doi: 10.47176/jafm.14.03.

[31] J. Kafle, P.R. Pokhrel, K.B. Khattri, P. Kattel, B.M. Tuladhar, and S.P. Pudasaini. Landslide-generated tsunami and particle transport in mountain lakes and reservoirs. *Annals of Glaciology*, 57(71):232–244, 2016. doi: 10.3189/2016AoG71A034.

[32] J. Kafle, B.K. Thakur, and I.B. Bhandari. Visualization, formulation, and intuitive explanation of iterative methods for transient analysis of series rlc circuit. *BIBECHANA*, 18:9–17, 2 2021. doi: https://doi.org/10.3126/bibechana.v18i2.31208.

[33] J. Kafle and B.M. Tuladhar. Landslide-water interaction for partially submerged landslide. *Journal of Nepal Mathematical Society*, 1(1):22–29, 2018.

[34] P. Kattel. *Dynamics of Quasi-Three-Dimensional and Two-Phase Mass Flows*. MPhil Dissertation, Kathmandu University, School of Science, Kavre, Dhulikhel, Nepal, 2014.

[35] P. Kattel. *Some Aspects of Multi-Phase Debris Flows: Dynamics, Flow-Obstacle-Interactions and Model Construction*. PhD thesis, Kathmandu University, School of Science, Kavre, Dhulikhel, Nepal, 2019.

[36] P. Kattel, J. Kafle, J.-T. Fischer, M. Mergili, B.M. Tuladhar, and S.P. Pudasaini. Interaction of two-phase debris flow with obstacles. *Engineering Geology*, 242, 2019. doi: 10.1016/j.enggeo.2018.05.023.

[37] P. Kattel, K.B. Khattri, P.R. Pokhrel, J. Kafle, B.M. Tuladhar, and S.P. Pudasaini. Simulating glacial lake outburst floods with a two-phase mass flow model. *Annals of Glaciology*, 57(71):349–358, 2016. doi: 10.3189/2016AoG71A039.

[38] P. Kattel and B.M. Tuladhar. Interaction of two-phase debris flow with obstacles. *Journal of Nepal Mathematical Society*, 1(2):40–52, 2018.

[39] K.B. Khattri. *Sub-diffusive and Sub-advective Viscous Fluid Flows in Debris and Porous Media*. MPhil Dissertation, Kathmandu University, School of Science, Kavre, Dhulikhel, Nepal, 2014.

[40] K.B. Khattri, P. Kattel, and B.M. Tuladhar. Some simulation results and parameter analyses of a generalized quasi two-phase bulk mixture model. *Journal of Nepal Mathematical Society*, 2(1):45–56, 2019.

[41] K.B. Khattri and S.P. Pudasaini. Channel flow simulation of a mixture with a full-dimensional generalized quasi two-phase model. *Mathematics and Computer in Simulations*, 165:280–305, 2019.

[42] G.-B. Kim. *Numerical simulation of Three-dimensional Tsunami Generation by Sub-aerial Landslides*. Master's Thesis, Texas A&M University, Texas, USA, 2012.

[43] H.M. King. What is a debris flow. *Geology. com*, 2017.

[44] S.I. De Lange, N. Santa, S.P. Pudasaini, M.G Kleinhans, and T. de Haas. Debris-flow generated tsunamis and their dependence on debris-flow dynamics. *Coastal Engineering*, 157:103623, 2020. https://doi.org/10.1016/j.coastaleng.2019.103623.

[45] F. Legros. The mobility of long-run out landslides. *Eng. Geol.*, 63(3-4):301–331, 2002.

[46] W. Liu, S. Yan, and S. He. A simple method to evaluate the performance of an intercept dam for debris-flow mitigation. *Engineering Geology*, 276:105771, 2020.

[47] G. Ma, J.T. Kirby, T.J. Hsu, and F. Shi. A two-layer granular landslide model for tsunami wave generation: theory and computation. *Ocean Modelling*, 93:40–55, 2015.

[48] G. Ma, F. Shi, and J.T. Kirby. Shock-capturing non-hydrostatic model for fully dispersive surface wave processes. *Ocean Modelling*, 43:22–35, 2012.

[49] M. Mergili, J.-T. Fischer, J. Krenn, and S.P. Pudasaini. r.avaflow v1, an advanced open-source computational framework for the propagation and interaction of two-phase mass flows. *Geosci. Model Dev.*, 10(2):553–569, 2017. doi:10.5194/gmd-10-553-2017.

[50] M. Mergili, B. Frank, J.-T. Fischer, C. Huggel, and S.P. Pudasaini. Computational experiments on the on the 1962 and 1970 mass flow events at Nevado Huascaran (Peru) with r.avaflow: Lessons learned for predictive mass flow simulations. *Geomorphology*, 322:15–28, 2018.

[51] F. Mohammed. *Physical Modeling of Tsunamis Generated by Three-dimensional Deformable Granular Landslides*. PhD Dissertation, Georgia Institute of Technology, 2010.

[52] F. Mohammed and H.M. Fritz. Physical modeling of tsunamis generated by three-dimensional deformable granular landslides. *Journal of Geophysical Research*, 117:705–718, 2012. C11015.

[53] T.S. Murty. Submarine slide-generated water waves in Kitimat Inlet, British Columbia. *Journal of Geophyical Research*, 84:7777–7779, 1979. doi: 10.1029JC084iC12p07777.

[54] J. S. O'Brien, P. J. Julien, and W. T. Fullerton. Two-dimensional water flood and mudflow simulation. *J. Hyd. Eng.*, 119(2):244–261, 1993.

[55] E. Pelinovsky and A. Poplavsky. Simplied model of tsunami generation by submarine landslide. *Phys. Chem. Earth*, 21(12):13–17, 1996.

[56] E.B. Pitman and L. Le. A two-fluid model for avalanche and debris flows. *Phil. Trans. R. Soc. A*, 363(3):1573–1601, 2005.

[57] P.R. Pokhrel, J. Kafle, P. Kattel, and H.P. Gaire. Analysis of blood flow through artery with mild stenosis. *Journal of Institute of Science and Technology*, 25:33–38, 2 2020. doi: https://doi.org/10.3126/jist.v25i2.33732.

[58] P.R. Pokhrel, K.B. Khattri, B.M. Tuladhar, and S.P. Pudasaini. A generalized quasi two-phase bulk mixture model for mass flow. *Int. J. of Non-Linear Mech.*, 99:229–239, 2018.

[59] P.R. Pokhrel, P.Kattel, K.B. Khattri, and J. Kafle. Rheological parameter analysis in generalized bulk mixture mass flow model. *The Nepali Math. Sc. Report*, 37(1), 2020.

[60] P.R. Pokhrel and S.P. Pudasaini. Stream function-vorticity formulation of mixture mass flow. *Int. J. of Non-Linear Mech.*, 2019.

[61] S.P. Pudasaini. A general two-phase debris flow model. *J. Geophysics. Res.*, 117(F03010), 2012. doi:10.1029/2011JF002186.

[62] S.P. Pudasaini. Dynamics of submarine debris flow and tsunami. *Acta Mechanica*, 225:2423–2434, 2014. doi:10.1007/s00707-014-1126-0.

[63] S.P. Pudasaini and K. Hutter. Rapid shear flows of dry granular masses down curved and twisted channels. *J. Fluid Mech.*, 295(193-208), 2003.

[64] S.P. Pudasaini and K. Hutter. *Avalanche Dynamics: Dynamics of Rapid Flows of Dense Granular Avalanches*. Springer, Berlin, New York, 2007.

[65] S.P. Pudasaini and M. Mergili. A multi-phase mass flow model. *Journal of Geophysical Research: Earth Surface*, 124:2920–2942, 2019.

[66] S.P. Pudasaini, Y. Wang, and K. Hutter. Modelling debris flows down general channels. *Nat. Hazards Earth Syst. Sci.*, 5:799–819, 2005.

[67] P. Sammarco and E. Renzi. Landslide tsunamis propagating along a plane beach. *J. Fluid Mech.*, 598:107–119, 2008.

[68] S.B. Savage and K. Hutter. The motion of a finite mass of granular material down a rough incline. *J. Fluid Mech.*, 199:177–215, 1989.

[69] S.B. Savage and K. Hutter. Dyanamics of avalanches of granular materials from initiation to runout. part i: Analysis. *Acta Mech.*, 86:201–223, 1991.

[70] N. Shuto. *Tsunamis of Seismic Origin*, pages 1–8. Springer Netherlands, 2003. doi=10.1007/978-94-010-0205-9_1.

[71] Y.-C. Tai, S. Noelle, J.M.N.T. Gray, and K. Hutter. Shock-capturing and front-tracking methods for granular avalanches. *J. Comput. Phys.*, 175(1):269–301, 2002.

[72] T. Takahashi. *Debris Flow*. IAHR-AIRH Monograph Series A, Balkema, Rotterdam, Netherlands, 1991.

[73] S. Viroulet, D. C'ebron, O. Kimmoun, and C. Kharif. Shallow water waves generated by subaerial solid land-slides. *Geophys. J. Int.*, 193:747–762, 2013. doi:10.1093gjiggs133.

[74] J.S. Walder, P. Watts, O.E. Sorensen, and K. Janssen. Tsunamis generated by subaerial mass flows. *J. Geophys. Res.*, 108(5):2236–2255, 2003.

[75] P. Watts. *Water Aves Generated by Underwater Landslides*. PhD. Dissertation, Calif. Institute of Technol., Pasadena, 1997.

[76] T. Xie, H. Yang, F. Wei, J.S. Gardner, Z. Dai, and X. Xie. A new water-sediment separation structure for debris flow defense and its model test. *Bull. Eng. Geol. Environ.*, 73:947–958, 2014. doi: 10.1007/s10064-014-0585-9.

[77] S. Yavari-Ramshe and B. Ataie-Ashtiani. Numerical modeling of subaerial and submarine landslide-generated tsunami waves-recent advances and future challenges. *Landslides*, 13(6):1325–1368, 2016.

[78] J. Zhai, L. Yuan, W. Liu, and X. Zhang. Solving the Savage-Hutter equations for granular avalanche flows with a second-order Godunov type method on GPU. *Int. J. Numer. Meth. Fluids.*, 77:381–399, 2015. doi: 10.1002/fld.3988.

[79] C. Zhang, J. T. Kirby, F. Shi, G. Ma, and S. T. Grilli. A two-layer non-hydrostatic landslide model for tsunami generation on irregular bathymetry. 2. numerical discretization and model validation. *Ocean Modelling*, 160:101769, 2021.